The Astrophysical Journal, 746:110 (26pp), 2012 February 10 doi:10.1088/0004-637X/746/1/110

CHALLENGES IN FORMING PLANETS BY GRAVITATIONAL INSTABILITY: DISK IRRADIATION AND CLUMP MIGRATION, ACCRETION, AND TIDAL DESTRUCTION

Zhaohuan Zhu[1,2], Lee Hartmann[1], Richard P. Nelson[3], and Charles F. Gammie[4,5]
[1] Department of Astronomy, University of Michigan, 500 Church St., Ann Arbor, MI 48109, USA; zhuzh@umich.edu, lhartm@umich.edu
[2] Department of Astrophysical Sciences, Princeton University, 4 Ivy Lane Peyton Hall, Princeton, NJ 08544, USA
[3] Astronomy Unit, Queen Mary, University of London, Mile End Road, London E1 4NS, UK; r.p.nelson@qmul.ac.uk
[4] Department of Astronomy, University of Illinois at Urbana-Champaign, 1002 W. Green St., Urbana, IL 61801, USA; gammie@illinois.edu
[5] Department of Physics, University of Illinois at Urbana-Champaign, 1002 W. Green St., Urbana, IL 61801, USA
Received 2011 July 13; accepted 2011 November 22; published 2012 January 27

ABSTRACT

We present two-dimensional hydrodynamic simulations of self-gravitating protostellar disks subject to axisymmetric, continuing mass loading from an infalling envelope and irradiation from the central star to explore the growth of gravitational instability (GI) and disk fragmentation. We assume that the disk is built gradually and smoothly by the infall, resulting in good numerical convergence. We confirm that for disks around solar-mass stars, infall at high rates at radii beyond $\sim$50 AU leads to disk fragmentation. At lower infall rates, however, irradiation suppresses fragmentation. We find that, once formed, the fragments or clumps migrate inward on typical type I timescales of $\sim 2 \times 10^3$ yr initially, but with a stochastic component superimposed due to their interaction with the GI-induced spiral arms. Migration begins to deviate from the type I timescale when the clump becomes more massive than the local disk mass, and/or when the clump begins to form a gap in the disk. As they migrate, clumps accrete from the disk at a rate between 10^{-3} and 10^{-1} M_J yr^{-1}, consistent with analytic estimates that assume a 1–2 Hill radii cross section. The eventual fates of these clumps, however, diverge depending on the migration speed: 3 out of 13 clumps in our simulations become massive enough (brown dwarf mass range) to open gaps in the disk and essentially stop migrating; 4 out of 13 are tidally destroyed during inward migration; and 6 out of 13 migrate across the inner boundary of the simulated disks. A simple analytic model for clump evolution explains the different fates of the clumps and reveals some limitations of two-dimensional simulations. Overall, our results indicate that fast migration, accretion, and tidal destruction of the clumps pose challenges to the scenario of giant planet formation by GI in situ, although we cannot address whether or not remnant solid cores can survive after tidal stripping. The models where the massive clumps are not disrupted and open gaps may be relevant to the formation of close binary systems similar to Kepler 16. A clump formed by GI-induced fragmentation can be as large as 10 AU and as luminous as 2×10^{-3} $L_\odot$, which will be easily detectable with ALMA, but its lifetime before dynamically collapsing is only $\sim$1000 years.

Key words: hydrodynamics – instabilities – planet–disk interactions – planets and satellites: formation – protoplanetary disks

Online-only material: color figures

1. INTRODUCTION

Even a small amount of rotation of a protostellar molecular cloud core will result in most of the core mass falling onto a disk rather than the central protostar. Unless non-gravitational angular momentum transport is very efficient or the initial angular momentum is very small, the resulting disk will become quite massive and subject to gravitational instability (GI; Vorobyov & Basu 2005, 2006; Rice et al. 2010; Zhu et al. 2010a), which can serve as an efficient mechanism to transport material inward (e.g., Durisen et al. 2007 and references therein). However, GI disks have been shown to be subject to fragmentation if the disk cooling time is shorter than or comparable to the orbital period (Gammie 2001; Rice et al. 2005; Paardekooper et al. 2011). Ignoring irradiation from the central star/accretion disk, this cooling criterion can be satisfied at radii beyond tens of AU (Nelson et al. 2000; Boley et al. 2006; Rafikov 2007; Stamatellos & Whitworth 2008; Stamatellos et al. 2011; Boley 2009; see Armitage 2011 for a review).

Gravitational fragmentation has been proposed as a mechanism to form giant planets beyond tens of AU (Boss 1997; Boley 2009), explaining recent observations of the presence of massive planets at large radii (e.g., Fomalhaut, Kalas et al. 2008; HR 8799, Marois et al. 2008). Alternatively, GI-induced fragmentation has been proposed to explain multiple star systems (Kratter et al. 2008, 2010a, 2010b; Offner 2011; Hayfield et al. 2011). On the other hand, GI fragmentation is complicated by the tendency of fragments to migrate inward; if they reach the star, they could produce jumps in accretion luminosity like those of FU Orionis outbursts (Vorobyov & Basu 2005, 2006; but see Zhu et al. 2010a, 2010b for an alternative model). If the migration stops at the inner disk, it may provide a formation mechanism for close binary systems (Section 7.1).

The variety of clump masses obtained in previous simulations suggests that GI-induced fragmentation depends on the initial condition of the disks, which should be determined by both the rate of infall and the mass of the growing central star. A more realistic treatment of GI requires consideration of both the way in which mass is loaded onto the disk as infall proceeds, and irradiation heating of the outer disk by the central star; the latter is known to weaken and/or suppress GI (Cai et al. 2008). Recent analytic studies (Levin 2007; Rafikov 2009; Cossins et al. 2010; Zhu et al. 2010a) have shown that irradiation may even suppress fragmentation beyond 50 AU. However, simulations with a large parameter space have not been carried out to confirm these analytic studies.

Investigations of the evolution of clumps have been limited so far largely because of numerical difficulties. Most three-

dimensional (3D) hydrodynamic simulations use arithmetically spaced computational grids in the radial direction, which can only cover a relatively small range of radii. Their limited resolution also makes it difficult to resolve the collapsing clump. Particle-based smoothed particle hydrodynamic (SPH) simulations can also suffer from deficient numbers of particles, especially in 3D (Nelson 2006). Many initial attempts to treat disk cooling in SPH simulations have only applied the orbital cooling prescription that leads to a runaway collapse. Recent studies have more realistic radiative transfer treatment implemented for both grid-based (e.g., Boley 2009) and SPH (e.g., Stamatellos & Whitworth 2008; Forgan et al. 2009; Forgan & Rice 2010; Boley 2009; Rogers & Wadsley 2011) calculations. But since 3D simulations are time consuming, long-timescale high-resolution simulations that can follow clump evolution are only feasible in two dimensions (2D). While some analytic work has been done (Nayakshin 2010a, 2010b, 2011) to explore long-term clump evolution, the migration process is simplified, and further mass growth through gas accretion is ignored once the clump has formed. Furthermore, 2D simulations enable us to study clump formation in a large parameter space of both disk and infall properties.

In order to study GI-induced disk fragmentation under the influence of both irradiation and mass infall, we have carried out high-resolution 2D hydrodynamic simulations with thermal physics included simply. We show how fragmentation depends upon the mass infall rate and the mass infall radius. Furthermore, with high-resolution long-timescale simulations, we are able to trace the clump evolution. We find that clumps migrate inward rapidly, unless they become massive enough to open gaps, and the accretion rate onto the clump is usually high due to the large cross section. Inward migrating clumps can be subject to tidal destruction as they migrate inward because of their shrinking Hill radii. But the detailed accretion physics around the clump and the dynamically unstable second core phase complicates this issue.

In Section 2, we introduce our numerical model. In Sections 3 and 4, we present our simulation results regarding disk fragmentation and clump evolution, in Section 5 we discuss the fate of the clumps, while in Section 6, we develop analytic models for disk fragmentation and clump evolution to compare with numerical results. The implications are discussed in Section 7, and conclusions are drawn in Section 8.

2. MODELS

We use the FARGO-ADSG code (Baruteau & Masset 2008) in a 2D (R, ϕ) fixed polar grid. FARGO-ADSG is an extended version of FARGO (Masset 2000), which uses a finite difference scheme with standard source and transport steps that are similar to ZEUS (Stone & Norman 1992). However, additional orbital advection has been applied which removes the average azimuthal velocity so that truncation error is reduced and the time step allowed by the Courant–Friedrichs–Lewy condition is significantly increased. Thus, FARGO-ADSG enables us to perform high-resolution simulations over long timescales. Furthermore, the effect of the central star acceleration due to the non-axisymmetric potential of the disk is included as an indirect potential term in the fluid equations (Baruteau & Masset 2008).

2.1. Radiative Cooling and Infall

Starting from the publicly available version of FARGO-ADSG, we have implemented the hydrodynamic equations with both a simplified radiative cooling treatment using detailed opacities (Appendix A, updated from Zhu et al. 2009b) and mass infall. The hydrodynamic equations are

$$\frac{\partial \Sigma}{\partial t} + \nabla \cdot (\Sigma v) = f_{\rm in}\,, \tag{1}$$

$$\Sigma\left(\frac{\partial v}{\partial t} + v \cdot \nabla v\right) = -\nabla P - \Sigma \nabla \Phi - \nabla \cdot \Pi + F_{\rm in}\,, \tag{2}$$

$$\frac{\partial E}{\partial t} + \nabla \cdot (E v) = -P \nabla \cdot v + Q^{+} - \Lambda_C + E_{\rm in}\,, \tag{3}$$

where Σ is the disk surface density, $E = \int e dz$ is the internal energy per unit area, $P = \int p dz$ is the vertically integrated pressure, Π is the viscous stress tensor (which is turned off in this paper), and v and Φ are the velocity and gravitational potential (including the self-gravity potential). v is constant along z and Φ is derived from the thin disk approximation. An ideal gas equation of state with $\gamma = 7/5$ has been assumed, so that $P = E(\gamma - 1)$. Then the averaged disk 2D temperature is $T_{\rm 2D} = P\mu/\Re\Sigma$, where $\Re$ is the gas constant. It can be shown that if $T(Z)^4 \propto T_0^4 \int \rho dZ$ in the vertical direction of a 3D disk, which is close to the structure of a viscous heating-dominated disk with a constant opacity, the disk's central temperature $T_c = 4/5 T_{\rm 2D}$, where $T_{\rm 2D}$ is calculated above with the total pressure and surface density. With irradiation included, $T_{\rm 2D}$ is closer to T_c, so we set $T_{\rm 2D} = T_c$. $f_{\rm in}$, $F_{\rm in}$, and $E_{\rm in}$ to model the effects of infall on the disk mass, angular momentum, and energy. These terms are described below in Equations (6)–(8).

The cooling rate per unit area, Λ_C, is modeled via

$$\Lambda_C = \frac{16}{3}\sigma\left(T_c^4 - T_{\rm ext}^4\right)\frac{\tau}{1+\tau^2}\,, \tag{4}$$

where $\tau = (\Sigma/2)\kappa_R(\rho_c, T_c)$ is the optical depth to the disk midplane at radius R. The Rosseland mean opacity $\kappa(\rho_c, T_c)$ is calculated using the opacity table given in Appendix A with the disk midplane density $\rho_c = \Sigma/2H$ and the midplane temperature T_c. The particular form $\tau/(1+\tau^2)$ is chosen so that the cooling term has the correct form in the optically thick and thin limits. (In the optically thin limit, κ should be the Planck mean opacity. Because the dominant opacity is from dust, which has a relatively slow variation with wavelength, we just use the Rosseland mean opacity for simplicity.)

The term $\sigma T_{\rm ext}^4$ represents the heating effect of the irradiation from the central star, assumed to vary as

$$T_{\rm ext}^4 = \frac{f(R) L_*}{4\pi R^2 \sigma}\,, \tag{5}$$

where L_* is the total luminosity of the star and $f(R)$ accounts for the normal component of the irradiation from the central star to the disk. Here we set $f(R)$ to have the constant value $f(R) = 0.1$, which is roughly what is expected for flared disks (Kenyon & Hartmann 1987; Chiang & Goldreich 1997; D'Alessio et al. 1998), and $L_* = L_\odot$. For disks without internal heating by spiral shocks, the temperature will relax to $T_{\rm ext}$ based on Equation (4).

The effect of infall onto the disk is represented by $f_{\rm in}$, $F_{\rm in}$, and $E_{\rm in}$ in Equations (1)–(3). $f_{\rm in}$ and $E_{\rm in}$ are the rates of disk mass and internal energy increase per unit area due to the infall, which can be directly derived from an envelope infall model. The form of $F_{\rm in}$, however, is less immediately apparent;

it is the equivalent shear force induced from merging infalling mass with the disk mass when they have different velocities. The relationship between $F_{\rm in}$ and the azimuthal velocity of the infalling envelope can be derived if we write the angular momentum equation from Equations (1) and (2):

$$\frac{\partial J}{\partial t} + \frac{1}{R}\left(\frac{\partial (v_\theta J)}{\partial \theta} + \frac{\partial (R v_R J)}{\partial R}\right) = -\frac{\partial P}{\partial \theta} - \Sigma \frac{\partial \Phi}{\partial \theta} + R(f_{\rm in} v_\theta + F_{{\rm in},\theta}), \quad (6)$$

where $J = \Sigma R v_\theta$. Thus, $R(f_{\rm in} v_\theta + F_{{\rm in},\theta})$ is the additional angular momentum brought by the envelope falling onto the disk per unit area, which should be $R f_{\rm in} v_{{\rm in},\theta}$, where $v_{{\rm in},\theta}$ is the azimuthal velocity of the infalling envelope as it lands on the disk at radius R. If the infalling envelope has the same velocity as the disk rotational velocity ($v_{{\rm in},\theta} = v_\theta$), there is no shear between the disk and the infalling envelope and $F_{{\rm in},\theta} = 0$.

In our simulations, we minimize the envelope's impact on the disk by assuming $F_{{\rm in},\theta} = 0$ in order to study the disk's response just to the mass loading from the infalling envelope. This is actually not a bad approximation based on the rigid rotating envelope infall model of Terebey et al. (1984) and Cassen & Moosman (1981), which suggests that most of the infalling material falls onto the centrifugal radius (R_c) where it has just slightly less than Keplerian rotation ($v_{{\rm in},\theta} \sim v_\theta$). This also implies $F_{{\rm in},R} = 0$. In our simulation we add mass to the disk within a small range in radii (R_a to R_b) according to

$$f_{\rm in}(R) = \frac{\dot{M}_{\rm in}}{2\pi R} \frac{(1-p) R^{-p}}{R_b^{1-p} - R_a^{1-p}} \quad (7)$$

so that by integrating over R_a to R_b the total infall rate is $\dot{M}_{\rm in}$. The parameter p is chosen to be 0.75 so that the disk within R_a and R_b has the same Q during the infall as if the disk is irradiation dominated (see Equation (5)). We also assume that the infalling material has a temperature equal to $T_{\rm ext}$ such that

$$E_{\rm in}(R) = f_{\rm in}(R) \frac{k_{\rm B} T_{\rm ext}}{(\gamma - 1)\mu {\rm m_H}}. \quad (8)$$

This is not precisely correct; backwarming from the envelope can actually heat the disk. We ignore this effect for simplicity in our simulations, but we discuss its possible impact in Section 7.2.

2.2. Initial Conditions and Simulation Setup

Currently, most simulations studying GI start with massive and non-irradiated disks. In such cases, the occurrence or otherwise of fragmentation depends upon the initial conditions (Boley 2009). Without external heating (irradiation), a disk with a finite initial temperature can cool to a point such that the Toomre parameter $Q \equiv c_{\rm s}\kappa/\pi G\Sigma \sim 1$, where κ is the epicyclic frequency, and the disk becomes gravitationally unstable. The equivalent orbital cooling time ($t_{\rm cool}$) sensitively depends on the initial surface density distribution:

$$t_{\rm cool}\Omega \sim \frac{\Omega E}{\sigma T_{\rm eff}^4}. \quad (9)$$

In the optically thick, the viscous heating-dominated case $T_{\rm c}^4 = (3/8) T_{\rm eff}^4 \tau$ and the cooling time becomes

$$t_{\rm cool}\Omega \sim \frac{\Omega \Sigma c_v T_c 3\Sigma C T_c^a}{\sigma 16 T_c^4} \propto \frac{1}{\Sigma^{4-2a} R^{10.5-3a}}, \quad (10)$$

where we have assumed that Q is constant to constrain the temperature, $\kappa_R = C T_{\rm c}^a$, where C is a constant, and the disk follows the Keplerian rotation law (so that $\kappa = \Omega = \Omega_K$) in obtaining the final proportionality relation. Since $a = 1.5$ for our grain opacity (Appendix A), larger initial surface densities at larger radii lead to shorter cooling times and fragmentation.

During a realistic star formation process, the disk is built up over a finite time from the infall of the parent molecular cloud core. Thus, the initial conditions depend on the mass and angular momentum distribution within the cloud, which can be quite complicated, and in any event are poorly constrained. Moreover, the thermal history of the disk can affect disk fragmentation (Clarke et al. 2007). To simulate the disk mass growth from infall until it becomes gravitationally unstable, we start with a relatively low-mass disk and then gradually add mass to the disk at a constant rate. When the disk becomes massive enough and gravitationally unstable, spiral arms generated by the GI will transport the infalling mass to the central star at a rate matching the infall rate if the system can achieve a steady state. With this procedure, we avoid strong relaxation at the beginning of our simulations which may cause fragmentation due only to initial conditions; this turns out to be important for simulation convergence as discussed in Section 2.3. It also allows us to control the infall rates and infall radii as two free parameters.

We have performed a variety of simulations with infall at different rates and radii. Since the disk undergoing GI tries to accrete to match the infall rate, $\dot{M} \sim \dot{M}_{\rm in}$ in order to maintain $Q \sim 1$, we can vary $\dot{M}_{\rm in}$ to control the disk accretion rate. These simulations are summarized in Table 1. Different cases are named as R+infall radii+infall rates. Thus, R40_3e-4 means the typical infall radii is 40 AU, while the infall rate at ~40 AU is $3 \times 10^{-4}\, M_\odot\, {\rm yr}^{-1}$. The special cases have notations after the infall rates that are self-explanatory or explained in the footnote. In the standard cases, the azimuthal grid resolution is 512. We use logarithmically spaced radial grids and choose the radial resolution such that every grid cell has the same azimuthal and radial size. In most of our simulations the radial resolution is ~400, with the inner radius at 5 or 10 AU and the outer radius at 1000 or 1500 AU (see Table 1). We set $f(R) = 0.1$ in Equation (5), so that $H/R \sim 0.029 (R/{\rm AU})^{0.25}$ (or $T_{\rm irr}(1\ {\rm AU}) = 215$ K with irradiation heating only). The initial disk surface density is $\Sigma = 4.16 \times 10^4 (R/{\rm AU})^{-1.75}$ g cm^{-2} with an exponential cutoff beyond R_b (obtained by multiplying the surface density by the factor $\exp(5 - 5R/R_b)$ if $R > R_b$, where R_b is defined in Equation (7)). With this setup, the disk is gravitationally stable ($Q \sim 2$) within R_b, and the disk surface density is extremely small close to the outer boundary at ~1000 AU. With infall, the disk gradually becomes gravitationally unstable near infall radii; spiral arms develop and start transporting mass inward, resulting in the inner disk gradually becoming gravitationally unstable.

We ran our simulations for up to 5×10^4 years for non-fragmenting cases. If the disk fragments, we run the simulation until a clump is close to the inner boundary and causes negative densities (details are given in Appendix B). (In the R200_3e-6 case we ran the simulation for 2×10^5 years to test whether this disk fragments on a longer timescale.) A timescale of 5×10^4 years is not much smaller than the estimated length of the infall phase for low-mass protostars, and is equivalent to 17 orbits at our largest infall radius (200 AU), long enough to see if the disk will fragment.

We assume that the central protostar has a fixed mass ($M_\odot$) throughout our simulations in order to study the disk response

Table 1
Models

Case Name	Resolution	$R_{\rm in}$ (AU)	$R_{\rm out}$ (AU)	Infall R_a (AU)	Infall R_b (AU)	$\dot{M}_{\rm in}$ ($M_\odot$ yr^{-1})	Time[a] (10^4 yr)	Fragments?	Color in Figures 8, 9, 10, and 11 and Comments
R40_3e-4	488 × 512	2.5	1000	25	40	3×10^{-4}	0.48	No	
R40_1e-4	488 × 512	2.5	1000	25	40	10^{-4}	0.4	No	
R65_3e-4	432 × 512	5	1000	50	65	3×10^{-4}	0.1	Yes	
R65_1e-4	432 × 512	5	1000	50	65	10^{-4}	1.24	Yes/M[b]	Red, clump A
R65_3e-5	432 × 512	5	1000	50	65	3×10^{-5}	2.04	No	
R65_1e-5	432 × 512	5	1000	50	65	10^{-5}	4	No	
R65_3e-6	432 × 512	5	1000	50	65	3×10^{-6}	4	No	
R100_3e-4	432 × 512	5	1000	85	100	3×10^{-4}	0.2	Yes	
R100_1e-4	432 × 512	5	1000	85	100	10^{-4}	0.67	Yes	Blue, clump B
R100_3e-5	432 × 512	5	1000	85	100	3×10^{-5}	2.4	Yes/M	Black, clump C
R100_1e-5	432 × 512	5	1000	85	100	10^{-5}	4	No	
R100_3e-6	432 × 512	5	1000	85	100	3×10^{-6}	4	No	
R200_3e-4	408 × 512	10	1500	175	200	3×10^{-4}	0.28	Yes	
R200_1e-4	408 × 512	10	1500	175	200	10^{-4}	0.47	Yes	
R200_3e-5	408 × 512	10	1500	175	200	3×10^{-5}	1.2	Yes	
R200_1e-5	408 × 512	10	1500	175	200	10^{-5}	3.3	Yes/M	Cyan, clump D,E,F,G
R200_3e-6	408 × 512	10	1500	175	200	3×10^{-6}	20	No	
Special Cases									
R100_1e-5I[c]	432 × 512	5	1000	85	100	10^{-5}	6.6	Yes/M	Green, clump H
R200_3e-5L100[d]	408 × 512	10	1500	175	200	3×10^{-5}	4	No	
R200_3e-6noirr[e]	408 × 512	10	1500	175	200	3×10^{-6}	8	Yes/M	Magenta, clump I,J,K
R100_1e-5DG1p57[f]	916 × 1024	10	1500	85	100	10^{-5}	4	No	
R200_1e-5G1p57[f]	816 × 1024	10	1500	175	200	10^{-5}	...	Yes	
R200_1e-5S0p06[g]	816 × 1024	10	1500	175	200	10^{-5}	...	Yes	
Resolution Studies									
R65_1e-5D	816 × 1024	10	1500	50	65	10^{-5}	3.6	No	
R65_3e-5D	816 × 1024	10	1500	50	65	3×10^{-5}	1.7	No	
R100_1e-5D	916 × 1024	10	1500	85	100	10^{-5}	3.96	No	
R100_1e-5D2	704 × 1024	20	1500	85	100	10^{-5}	4	No	
R100_1e-5Q2	1408 × 2048	20	1500	85	100	10^{-5}	2.65	No	
R200_1e-5	816 × 1024	10	1500	175	200	10^{-5}	3.3	Yes	

Notes.
[a] If fragmentation occurs, this gives the time when the first clump migrates to the inner boundary.
[b] These are the marginal fragmentation cases where only one or two clumps form in the disk.
[c] Decreasing irradiation after 5×10^4 yr.
[d] Luminosity is 100 $L_\odot$ from the central star.
[e] No irradiation included.
[f] The same as the corresponding case in the resolution studies but with $\gamma = 1.57$ instead of 1.4.
[g] The smoothing length is 0.06 disk scale height at 5 AU, compared with other cases with 0.6 disk scale height smoothing length at 5 AU.

to the mass infall only. Thus our simulations are approximating the disk evolution near the end of protostellar collapse, when the central object is quite massive and emits significant radiation. The expected mass of the GI disk from $R_{\rm in}$ to $R_{\rm out}$ can be estimated by assuming $Q = 1$ with the temperature set by our irradiation prescription (Equation (5)):

$$M_d = 0.22 \left(\left(\frac{R_{\rm out}}{\rm AU} \right)^{0.25} - \left(\frac{R_{\rm in}}{\rm AU} \right)^{0.25} \right) M_\odot. \quad (11)$$

With $R_{\rm out} = 100$ AU and $R_{\rm in} = 10$ AU, we have $M_d = 0.3 M_\odot$. Thus, the disk is massive compared with the central star if irradiation is considered.

To study how irradiation affects fragmentation, we ran three additional simulations with high, low, and no irradiation. The high irradiation case, R200_3e-5L100, is similar to R200_3e-5 but with 100 $L_\odot$, typical of an A-type star. On the contrary, the decreasing irradiation case, R100_1e-5I, is similar to case R100_1e-5, but after 5×10^4 years, with the same infall rate, the irradiation parameter in Equation (5) gradually decreases at a rate

$$f(R) = 0.1 \left(1 - \frac{t}{5 \times 10^4 \ {\rm yr}} \right)^8, \quad (12)$$

until the disk fragments. Equation (12) is chosen so that the disk scale height due to irradiation decreases linearly with time and the disk mass decreases linearly with time (assuming Q = constant). The resulting mass accretion rate due to the decreasing irradiation is much smaller than the infall rate at $R > 85$ AU, so the disk accretion rate is still controlled by the infall rate. Finally, we performed one simulation similar to R200_3e-6 but without irradiation at all, which is labeled as R200_3e-6noirr. The entire suite of parameters explored in our simulations is summarized in Table 1.

2.3. Numerical Tests

To explore how robust our simulations are, we have carried out simulations with different settings. The most important issue

is the convergence on the fragmentation criterion raised by Meru & Bate (2011). Some other issues include the γ value and the gravitational force smoothing length.

2.3.1. Resolution Tests

To study whether the critical fragmentation radius depends on the numerical resolution, we have re-calculated several marginal fragmentation and non-fragmentation cases, but with double the resolution in both radial and azimuthal directions as shown in Table 1. Non-fragmentation cases remain non-fragmenting at higher resolution and the fragmentation case still fragments. A particular concern applies to the non-fragmentation case, in which numerical dissipation may prevent disk fragmentation. Thus, for the R100_1e-5 case, we double and even quadruple the resolution in both radial and azimuthal directions, but the disk still remains non-fragmenting. We want to point out that the irradiated disk has a larger scale height which is better resolved numerically. We conclude that an azimuthal resolution of 512 cells is enough to study disk fragmentation, which is expected considering each disk scale height is resolved by 7.5 grid cells at 100 AU (considering $H/R \sim 0.029(R/\mathrm{AU})^{0.25}$) and the neutral stability critical wavelength ($L = 2\pi H$ for $Q = 1$) is resolved by 45 grid cells, far larger than that required by the condition given in Nelson (2006).

Recent SPH simulations by Meru & Bate (2011) have questioned the convergence of the orbital cooling fragmentation criterion for GI disks. However, in our resolution tests from 512 to 2048 azimuthal grid cells and the corresponding quadruple resolution increase in the radial direction, our results converged for both non-fragmenting and fragmenting disks. We attribute this discrepancy to the fact that we gradually build the disk from a gravitationally stable state to an unstable state by adding mass to the disk. This process not only simulates the real astronomical condition of infall but also allows the disk to regulate itself. In a sense this is similar to Clarke et al. (2007), who increased disk cooling gradually. Simulations by Paardekooper et al. (2011) confirmed that the treatment in Clarke et al. (2007) leads to a convergent cooling criterion, which is consistent with our finding that gradually built-up disks converge.

2.3.2. Adiabatic Index

The 2D adiabatic index γ is related to the 3D Γ in the static limit (e.g., Goldreich et al. 1986). In a strongly self-gravitating disk, $\gamma = 3 - 2/\Gamma$. If the 3D $\Gamma = 1.4$, the 2D $\gamma = 11/7 \sim 1.57$. We explore both the quasi-steady GI and highly dynamic fragmenting states, so it is not obvious what γ value we should choose. We have simulated two cases, non-fragmenting and fragmenting disks, with both $\gamma = 1.4$ and 1.57 (Table 1). Our results suggest that the fragmentation criterion does not depend sensitively on γ in the range from 1.4 to 1.57. This is consistent with Rice et al. (2005). On the other hand, Boley et al. (2007) have found that the variation of γ due to thermalization of the rotational levels of molecular hydrogen can affect GI (Boley et al. 2007). In our already simplified 2D simulations, however, we simply assume γ is constant.

2.3.3. Gravitational Force Smoothing Length

To avoid small-scale density fluctuations leading to a runaway collapse, we use a smoothed gravitational force (Baruteau & Masset 2008). Considering that the disk vertical structure can smooth the disk's global gravitational potential, we assume a smoothing length of 0.0264 R, which is 0.6 disk scale height at 5 AU and 0.3 disk scale height at 100 AU. Since a large smoothing length may lead to bigger clumps, we have carried out one simulation with smoothing length 10 times smaller. The clump mass from this simulation turns out to be close to the clump mass from the corresponding large smoothing length simulation. This is consistent with Baruteau et al.'s (2011) finding that a small smoothing length does not change the properties of the gravo-turbulence.

3. RESULTS: FRAGMENTATION

Images of the disk surface density for models with different infall rates and infall radii at intermediate times are shown in Figure 1. In this figure, the infall rate increases horizontally from $3 \times 10^{-6}\,M_\odot\,\mathrm{yr}^{-1}$ (left) to $3 \times 10^{-4}\,M_\odot\,\mathrm{yr}^{-1}$ (right). The infall radius runs vertically from 65 AU (top) to 200 AU (bottom). These runs are listed from R65_3e-4 to R200_e3e-6 in Table 1. At a given infall rate (moving from top to bottom down a column in Figure 1), the spiral arms become narrower and more unstable with increasing infall radius and eventually break into fragments. At marginal fragmentation only one clump forms, while for a more unstable case, several clumps form simultaneously. Higher infall rates at the same radius (moving from left to right along a row in Figure 1) also lead to more unstable spiral arms. Similarly, fragmentation becomes more severe (one clump to multiple clumps) with higher infall rates at the same radius. The critical radius where the disk starts to fragment increases with decreasing infall rate (marginal fragmentation cases form a diagonal line in Figure 1 moving from top right toward bottom left).

Figure 2 summarizes our fragmentation results, and they are in approximate agreement with our previous analytic estimates for the critical radius for fragmentation as a function of the mass infall rate (Zhu et al. 2010a, and further details in Section 6). These estimates are shown as curves in Figure 2.

The special case R100_1e-5I (decreasing irradiation) is shown in Figure 3. This disk fragments at $R = 400$ AU when $f(R)$ decreases to 0.013. A comparison simulation that maintains full irradiation (run R100_1e-5), which is shown in the lower right panel of Figure 3, does not fragment. We thus confirm that irradiation tends to suppress fragmentation at a fixed infall rate. In the zero irradiation limit model R200_3e-6noirr fragments, unlike its counterpart with full irradiation, which again confirms that irradiation suppresses the fragmentation.

In the high irradiation limit (run R200_3e-5L100) the disk did not fragment by the end of our simulation (5×10^4 years), unlike its $1\,L_\odot$ counterpart. Again, irradiation suppresses fragmentation. This also suggests that for high-luminosity systems (where $L \sim 100\,L_\odot$) GI can transfer mass inward smoothly from hundreds of AU; an analytic treatment of this result is given in Section 6.1.

4. RESULTS: CLUMP EVOLUTION

In a fragmenting disk, clump formation and evolution should resemble protostar formation and evolution (Larson 1969; Bodenheimer et al. 1980). During disk/cloud fragmentation, a quasi-hydrostatic core forms (this stage is called the "first core" in protostellar studies). When the core's central temperature rises from ~1500 to 2000 K, the dust sublimates, and then hydrogen molecules begin to dissociate. At this point the ratio of specific heats γ decreases below 4/3, the clump becomes dynamically unstable and collapses to form the so-called second core (Larson 1969).

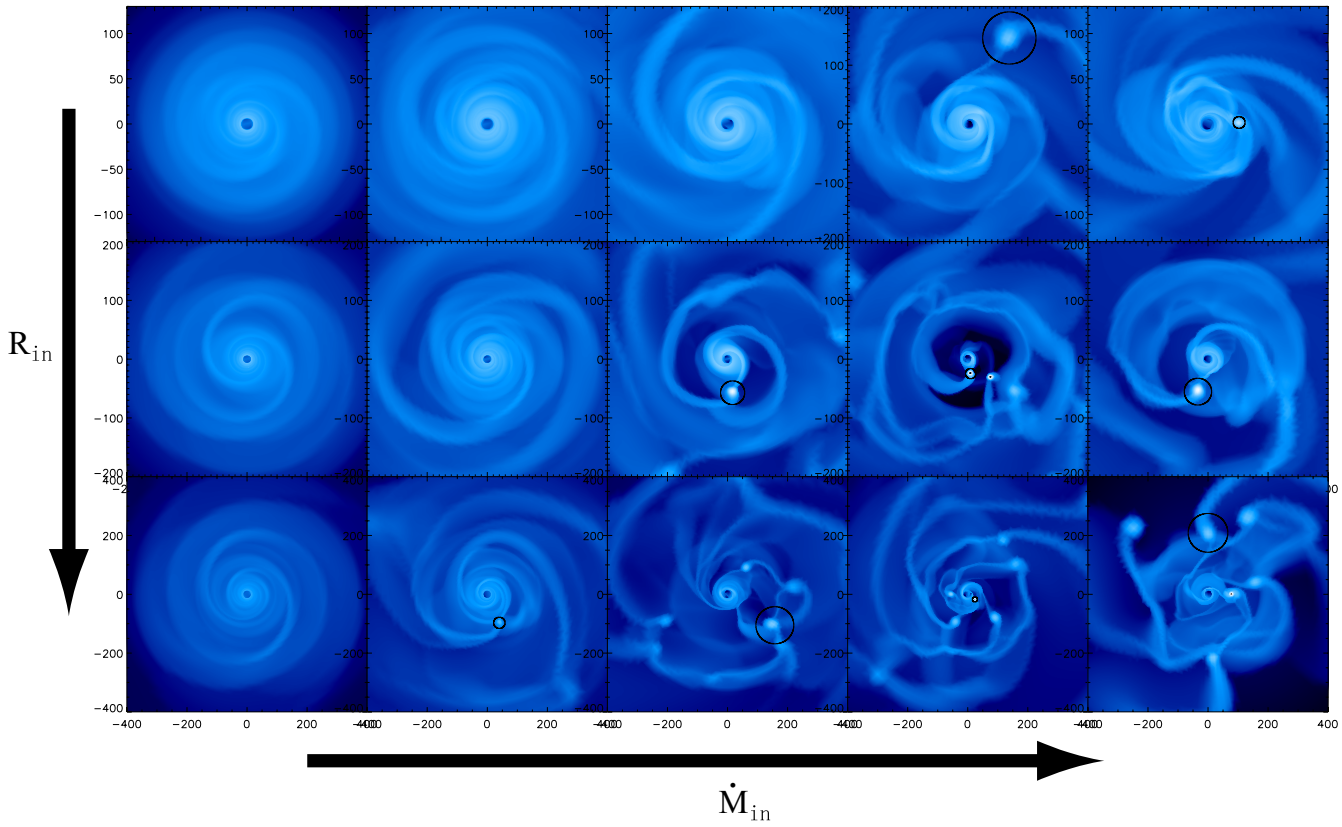

Figure 1. Disk surface density distribution at the end of the simulations (time shown in Table 1) with different infall rates (increasing from $3 \times 10^{-6}\ M_\odot\ \mathrm{yr}^{-1}$ on the left to $3 \times 10^{-4}\ M_\odot\ \mathrm{yr}^{-1}$ on the right) and infall radii (65 AU, 100 AU, and 200 AU from the top to bottom). The black circle labels the Hill radius of the selected clump if the disk fragments.

(A color version of this figure is available in the online journal.)

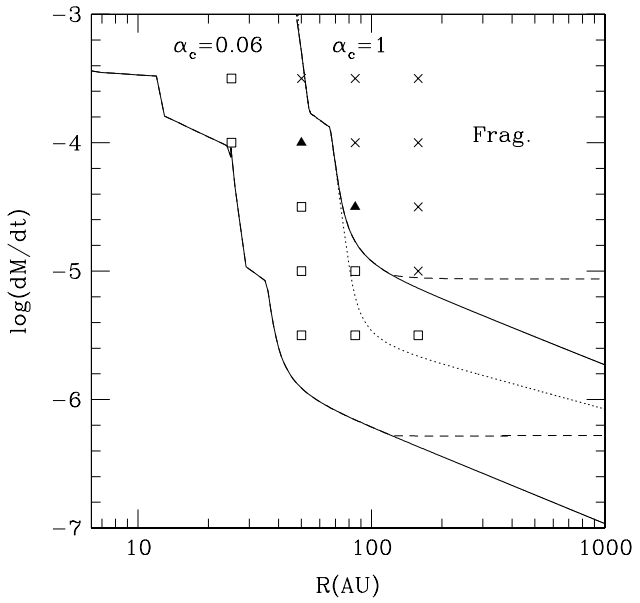

Figure 2. Fragmentation radii for gravitationally unstable disks with different infall rates (in units of $M_\odot$/yr). Analytical estimates are shown with the critical fragmentation viscosity parameter $\alpha_c = 0.06$ (left solid curve) and $\alpha_c = 1$ (right solid curve). The dotted curve represents the fragmentation radii without irradiation ($\alpha_c = 1$ is assumed). The dashed curves represent the same estimates but with the minimum irradiation temperature set to 20 K. Crosses label the disks fragmenting with multiple clumps, while the solid triangles label the disk that only has one or two clumps (marginally fragmentation cases). Open squares label the disks that fail to fragment and can accrete steadily.

In our 2D simulations we cannot simulate the dynamically unstable "second core," and whenever dust sublimates at the midplane our assumption that the disk has uniform opacity vertically becomes invalid. Thus, although we allow the clump to be heated up above 1500 K, our results at those stages are not accurate. Whenever the clump is above 2000 K and the center of the clump has collapsed to the "second core," a circum-clump disk will form, and its accretion becomes important for the clump's further growth. In this paper, we focus on the "first core" stage. Even for this stage, we found there are three distinct fates for the clumps. During the clump's inward migration, if the clump grows massive enough to open a gap, it slows down or even stops migration. On the other hand, if the clump fails to open a gap, continuous migration can eventually lead to tidal destruction. There is a third possibility that the clump manages to migrate inward all the way to the central star without being tidally destroyed. Since our inner boundary is at $\sim$10 AU, we cannot follow the clump all the way to the central star to confirm this possibility, but provide further analytic estimates to investigate this in Section 6.2. Nonetheless, our simulations do exhibit clumps that manage to reach the inner boundary of the computational domain without being tidally disrupted.

We want to emphasize that all the clumps studied hereinafter are limited to the marginally fragmentation cases, in which only one or two clumps form in the disk. They do not suffer the strong clump–clump scattering seen in cases of multiple fragmentation, which complicates their evolution.

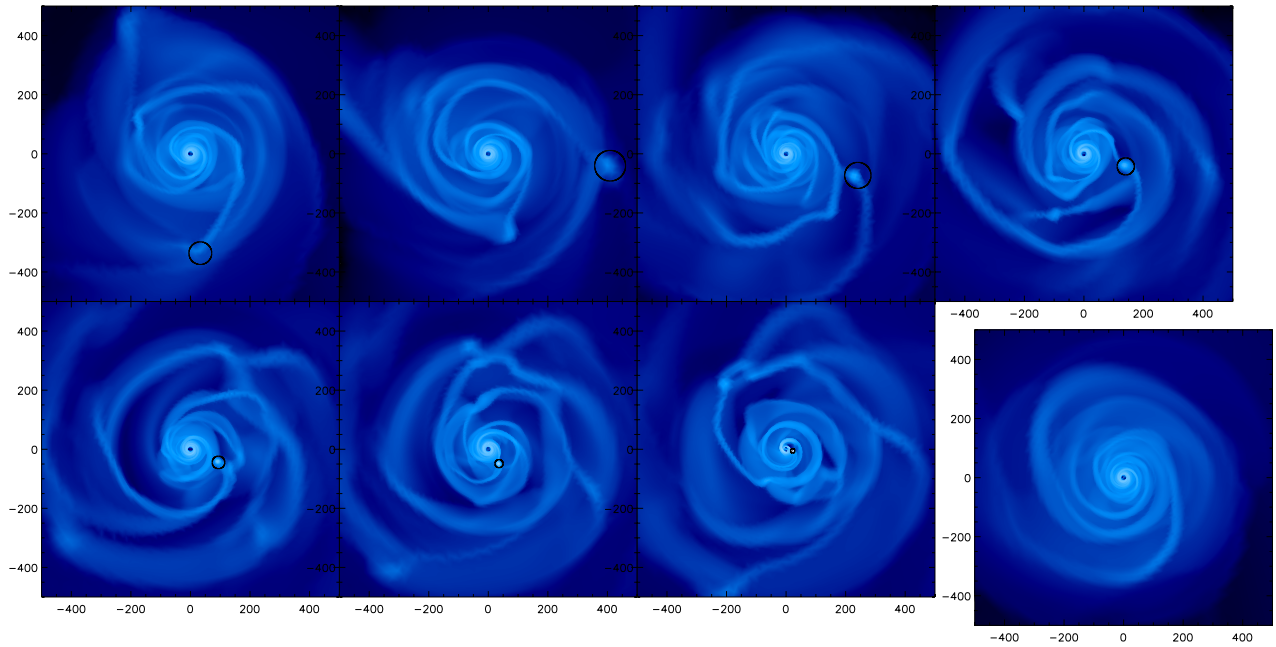

Figure 3. Clump formation and migration for the R100_1e-5I (decreasing irradiation) case compared with the R100_1e-5 case (lower right panel). For the R100_1e-5I case, the upper left panel shows the clump formation and then each consecutive panel shows the clump one orbital period later (5.78, 5.89, 6.27, 6.44, 6.53, 6.57, 6.61 $\times$ 10^4 years after the start of the simulation). After five orbits the clump moves from 300 AU to 10 AU. The black circle labels the Hill radius of the clump.
(A color version of this figure is available in the online journal.)

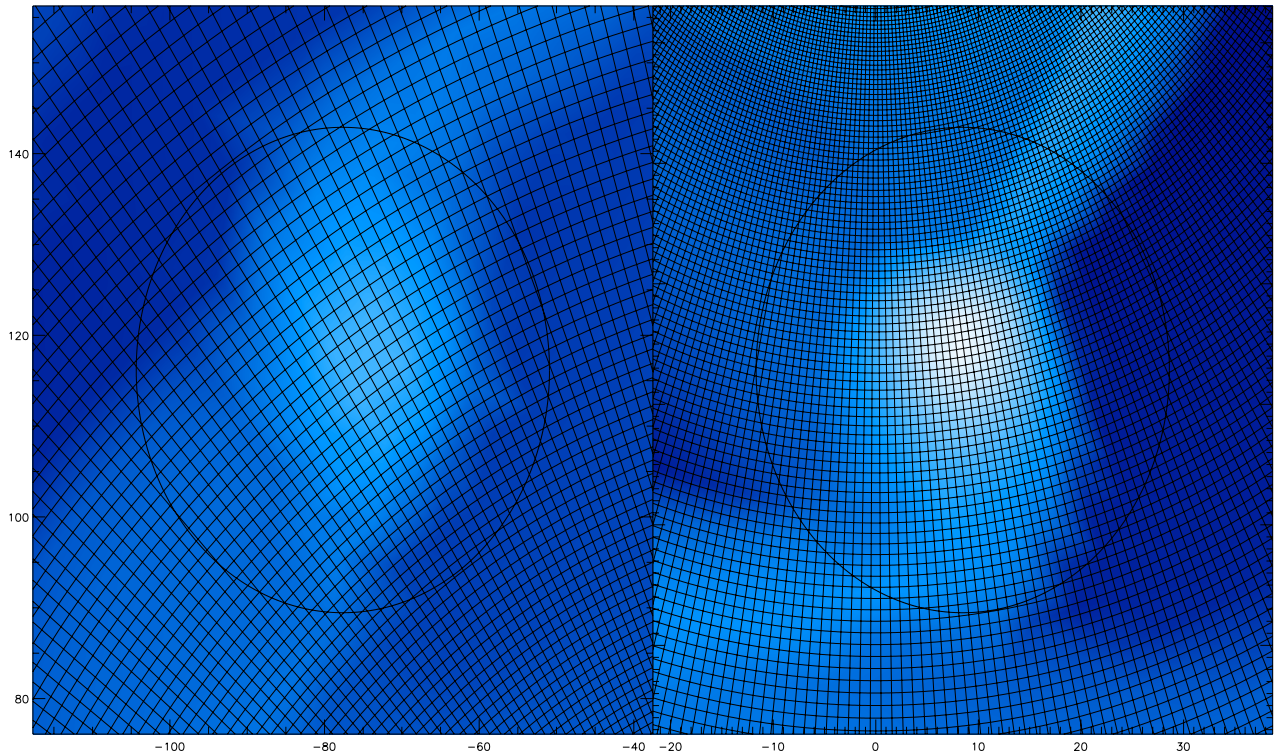

Figure 4. Surface density of the clump (run R100_3e-5) that just forms (2.2 $\times$ 10^4 years after the start of the simulation, left panel) and fully developed (2.4 $\times$ 10^4 years after the start of the simulation, right panel). The black circle labels the Hill radius of the clump and the numerical grids have been plotted on top of the density distribution.
(A color version of this figure is available in the online journal.)

4.1. Clump Structure

Figure 4 shows the clump from the run R100_3e-5 with the numerical grid overlaid on the surface density distribution. The left panel shows the clump when it first forms at 150 AU after 2.2 $\times$ 10^4 years, and the right panel shows its density 2000 years later when it has migrated in to 50 AU. The clump is well resolved at both times.

Figure 5 shows the temperature distribution of the clump (corresponding to the right panel of Figure 4). Velocity vectors are superimposed showing the velocity field measured in a frame rotating at the same rate as the center of the clump.

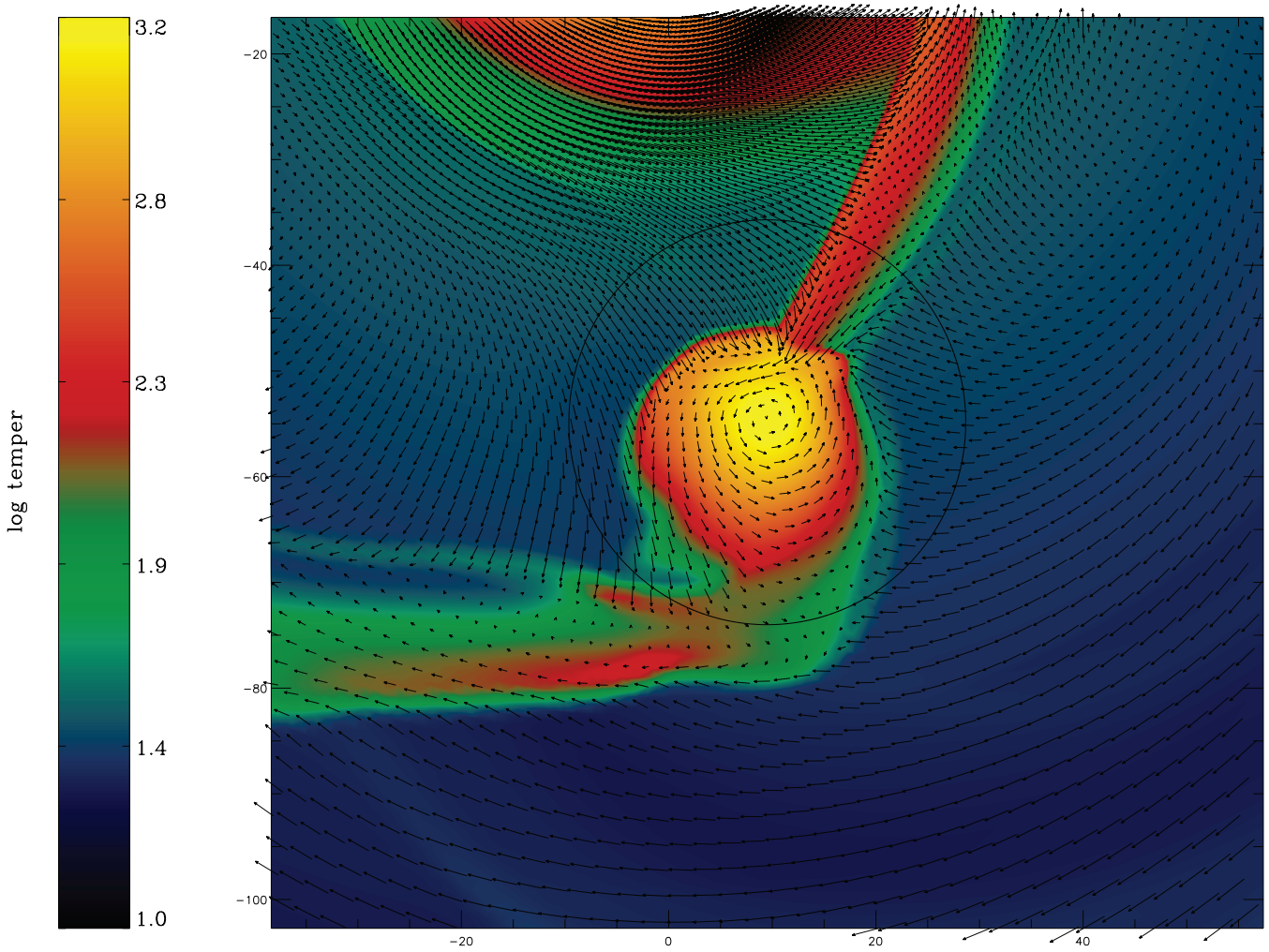

Figure 5. Midplane temperature distribution of the clump as shown in the right panel of Figure 4 plotted with velocity vectors in the frame corotating with the clump center.

(A color version of this figure is available in the online journal.)

Shocked regions form at the edges of the clump where the infalling material from the disk collides with the pressure-supported clump (a similar phenomenon is observed in the 1D simulations by Larson 1969). As the clump accretes gas with high relative angular momentum, it develops significant rotation (2 km s^{-1}, compared with the Keplerian rotation speed of 4 km s^{-1} in the clump rotating reference frame, as discussed in detail below). The prograde clump rotation is similar to that seen in simulations of circumplanetary disks (Lubow et al. 1999), presumably because of a similar flow pattern occurring as gas enters the clump Hill sphere from the surrounding protostellar disk. This is also consistent with the results of Vorobyov & Basu (2010) and Boley et al. (2010).

The clump's structure at the different times shown in Figure 4 is revealed in detail in Figure 6. The clump's central density and temperature increase with time during the collapse of the clump. For a hydrostatic core, the clump's self-gravity should be balanced by the sum of the pressure and centrifugal forces due to the clump's rotation. When the clump first collapses, it collapses radially until it is pressure supported. Since at this early stage little mass has been accreted that adds angular momentum to the clump, the clump rotates slowly. The pressure gradient $\partial P/\partial R$ then balances the clump's self-gravity and is almost one order of magnitude larger than the centrifugal force (the left panel of Figure 4). Later, loss of thermal energy due to radiative cooling leads to further clump contraction, and the clump spins up. Disk mass with high specific angular momentum is also accreted, increasing the rotation of the clump, and centrifugal force becomes comparable to the pressure gradient as shown in the right panels of Figure 6. In order to qualitatively estimate how much angular momentum is brought by the accreted gas from the disk, an analogy can be drawn between accreting giant planets in disk gaps and our accreting clumps. Ayliffe & Bate (2009) have shown that the accreted gas from the disk falling onto the planet forms a circumplanetary disk with a radius 1/3 of the planet's Hill radius. Thus, if the angular momentum of the accreted gas dominates our clump's initial angular momentum, our clump is expected to be close to or even larger than 1/3 of the planet's Hill radius considering the clump is also partly pressure supported. This is confirmed in our simulations, shown below, where our clump radii are close to half their Hill radii.

To study clump evolution further, we define a clump mass, M_c, and radius, r_c, as follows. First, we choose a large circle around the clump and integrate the total mass. If the Hill radius $r_H = R(M_c/3M_*)^{1/3}$ calculated by this mass is larger than the initial radius of the circle, we choose a smaller circle by iteration until the Hill radius is the same as the radius of the circle. Then we define the clump center as the position of peak surface density

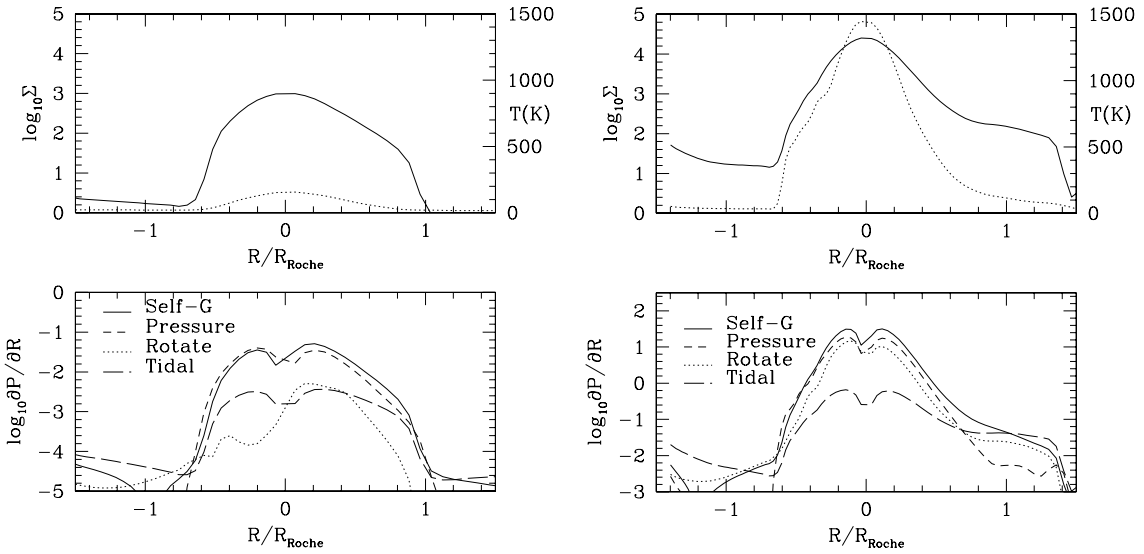

Figure 6. Clump's surface density (dotted curve) and temperature (solid curve) profile along the radial cut across the clump center (upper panels) at the two different times corresponding to the left and right panels of Figure 4. Lower panels show various forces along this cut. In the left panels the rotational support is negligible, while in the right panels the rotational support is as important as the thermal support.

and we compute the average disk surface density Σ_H around the circumference of the clump's Hill radius. After this step, we look for the closed curve $r(\theta)$ around the clump center where its surface density is equal to $0.5 \times (\log_{10}\Sigma_H + \log_{10}\Sigma_{\rm max})$, where $\Sigma_{\rm max}$ is the surface density at the clump center. We then define the clump radius as the average distance from the curve to the clump center ($r_c = \int r(\theta) d\theta/2\pi$, where θ is the angle between the line connecting each position on the curve and the clump center with respect to a reference direction, taken to be the line joining the central star to the clump). This clump radius can be used to determine whether or not the clump can be tidally destroyed, by comparing it with the Hill radius, which will be discussed in detail in Section 5.2.

Quantitatively, the clump in the left panel of Figure 4 for the R100_3e-5 case is at 139 AU with mass 0.026 $M_\odot$ and Hill radius 26 AU. The total specific angular momentum J with respect to the clump center is 4×10^{17} cm^2 s^{-1} which is similar to Boley et al. (2010). When the clump accretes mass, both mass and angular momentum increase. For the clump in the right panel of Figure 4, its mass is 0.159 $M_\odot$ (the upper panel in Figure 7) and the specific angular momentum is 10^{19} cm^2 s^{-1}. Such high specific angular momentum can limit contraction of the clump even in the "first core" stage. For an order of magnitude estimate, the clump in the right panel cannot contract to become smaller than ~AU scale. This is roughly consistent with the 8 AU clump radius calculated using the procedure defined in the last paragraph. Even with the significant growth in mass, the core radius remains approximately half the Hill radius at all times, as shown by the right-hand vertical axis in the middle panel of Figure 7. However, the angular momentum distribution within a clump and how it is transported outward is unclear. We do not include explicit viscosity in these simulations, so evolution of the clump spin angular momentum distribution can arise through tides and numerical diffusion.

Considering that the clump's dynamical timescale (free-fall timescale) is significantly shorter than its Kelvin–Helmholtz timescale (Nayakshin 2010a), the clump can be approximated as quasi-hydrostatic during its collapse (more timescale estimates are discussed in Section 5.2). This is confirmed by the bottom panel of Figure 7 where $GM_c/\Re r_c T_c \sim 1.5$ is almost constant

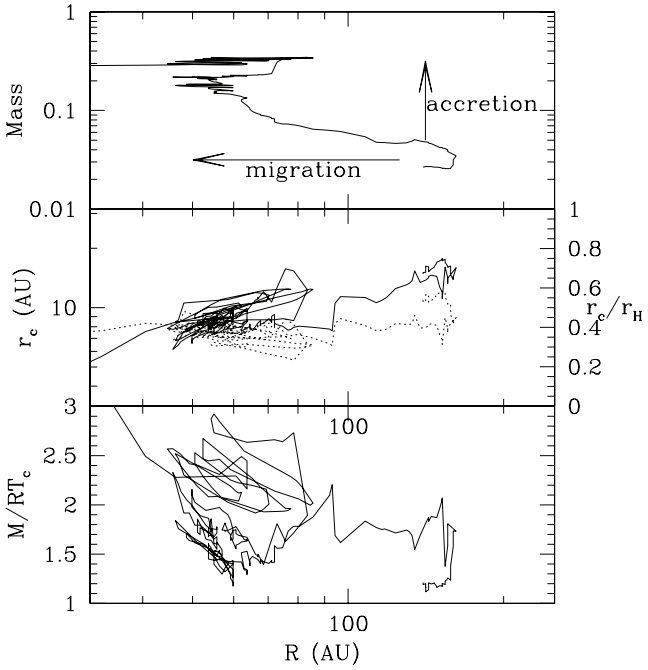

Figure 7. Clump's mass (in unit of solar mass), core radius (solid curve), r_c/r_H (dotted curve), and $GM_c/\Re T_c$ with the clump's position in the disk for the R100_3e-5 case.

throughout the clump evolution. As shown in Equation (C7) in Appendix C, for a spherical, hydrostatic, radiative clump, we expect $GM_c/\Re r_c T_c \sim 0.7$. However, considering the rather rough definition of r_c in our 2D simulation, the geometric difference between 2D and 3D, and using the disk midplane opacity to represent the envelope opacity at that disk radius, a factor of two uncertainty is expected and can be roughly considered as our error bar.

4.2. Clump Accretion

In the previous subsection, we explored clump structure by following an individual clump. From this subsection, we will

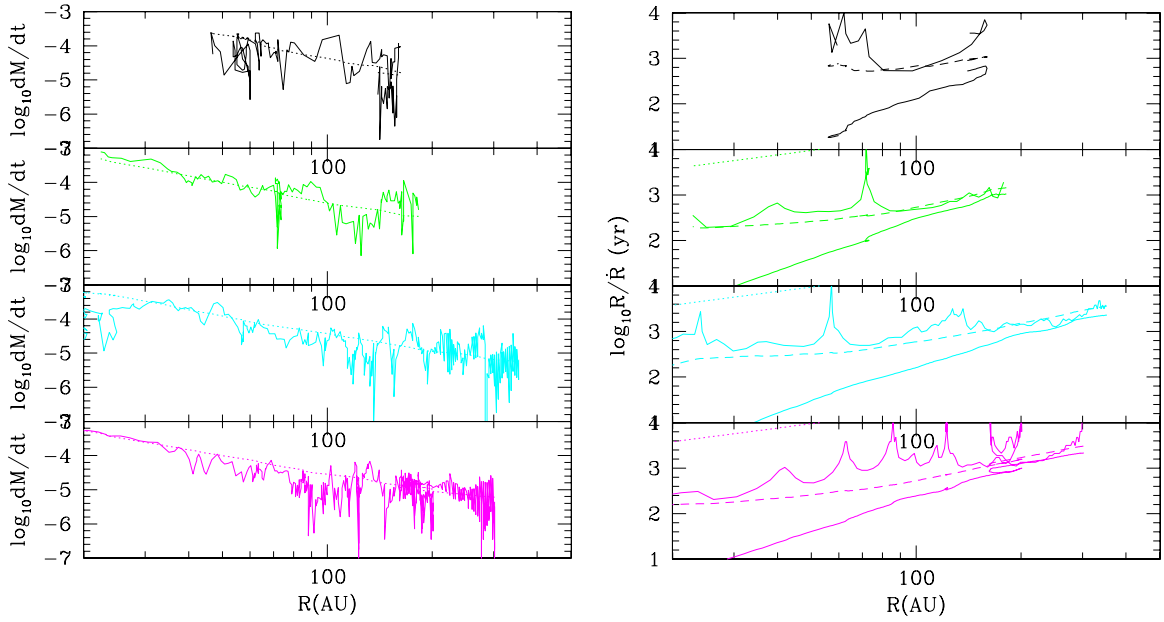

Figure 8. Left: the clump mass accretion rate (in units of $M_\odot$/yr) when the clump migrates inward in the disk. Reading from the top, we show cases R100_3e-5 (clump C), R100_1e-5I (clump H), R200_1e-5 (clump D), and R200_3e-6noirr (clump K); different colors correspond to the cases described in Table 1. The dotted lines show the analytic estimates based on Equation (15). Right: the migration timescale in years $R/\dot{R}$ at each radius for the same cases. The lower solid curves show the type I migration timescales estimated with Equation (16), while the upper dotted curves show the type II migration timescales with $\alpha = 1$. The dashed curves show our fit using Equation (18).

(A color version of this figure is available in the online journal.)

study general clump evolution (e.g., accretion and migration). After the disk starts fragmenting, a clump quickly evolves to a quasi-hydrostatic state. As shown in the previous section, the core radius is approximately half of the Hill radius, leaving plenty of space for disk material to accrete onto the collapsed clump. Due to the stochastic nature of the clump accretion and migration in GI disks, we will follow the clumps from a number of disk fragmentation cases to increase our sample.

Clump accretion rates as a function of time are shown in the left panel of Figure 8. They vary from $10^{-5}\,M_\odot\,\mathrm{yr}^{-1}$ at 200 AU to $10^{-4}\,M_\odot\,\mathrm{yr}^{-1}$ at tens of AU. These accretion rates can be estimated by assuming that the accretion cross section corresponds to 1–2 clump Hill radii:

$$\dot{M}_c = 2\Sigma \int_0^{x_{\max}} dx\, v_{\mathrm{shear}}, \tag{13}$$

where $v_{\mathrm{shear}} = 3/2\Omega x$, $x = R - R_{\mathrm{clump}}$, and R_{clump} is the clump's radial position in the disk. $x_{\max}$ corresponds to the impact parameter where the last unbound orbit sits. This impact parameter has been studied in the context of planetary rings by Petit & Henon (1986) and Henon & Petit (1986), and in giant molecular cloud scattering by Gammie et al. (1991). We can understand the gas flow in a gaseous Keplerian rotating disk by applying the results from the circular restricted three-body problem. If disk material is orbiting at a radius very close to the clump (small impact parameter), the Jacobi integral is large and the disk material is restricted to the horseshoe region in the vicinity of the corotation radius. If disk material orbits far from the clump, it will follow its Keplerian orbit with very little perturbation from the gravity of the clump. Only disk material with intermediate impact parameters can be captured. The impact parameter of the last unbound orbit as in Equation (13) normally lies between 1 and 2 Hill radii (Gammie et al. 1991; Bryden et al. 1999; Lubow et al. 1999). The planet–disk interaction studies of Bryden et al. (1999) and Lubow et al. (1999) have clearly demonstrated how the planet accretes from the gaseous disk. Although spiral shocks complicate the orbits of the disk material, gas in the circumstellar disk orbiting 1–2 Hill radii away from the planet is deflected into the Hill sphere by the planet's gravity. In a disk undergoing GI, the clump forms within a high density spiral arm, and mass can also flow along this arm onto the clump, as indicated in Figure 5. Even with this further complication, we find that Equation (13) can describe the accretion rate onto a clump accurately.

Assuming $x_{\max} = f_c r_H$, we can estimate

$$\dot{M}_c = \frac{3}{2}\Sigma\Omega(f_c r_H)^2\,, \tag{14}$$

where higher order terms in x/R are neglected. Because the disk surface density fluctuates vigorously with time and the migration is stochastic, the accretion rate onto the clump also fluctuates. Comparing Equation (14) with our simulations, we found $f_c \sim 1.7$, and

$$\dot{M}_c = 4\Sigma\Omega r_H^2\,, \tag{15}$$

in basic agreement with the discussion above. With our parameter it is $\dot{M}_c = 1.7 \times 10^{-5}\ (R/100\,\mathrm{AU})^{-1.25}\ (M_c/10\,M_J)^{2/3} M_\odot/\mathrm{yr}$. This equation shares a similarity with the planet accretion rate from D'Angelo & Lubow (2008), but in our cases the Hill radius is larger than the disk scale height and the cross section is $\sim r_H$ instead of $\sim r_H^2$. Accretion rates obtained from the simulations, and estimated using Equation (15), are shown in the left panel of Figure 8. In our simulations, the accretion rates are higher than what Boley et al. (2010) assumed. We think this is due to the effect equivalent to gravitational focusing. When the flow passes around the planet, it is gravitationally focused to the planet so that its cross section increases (Figure 5). Clearly this result is only valid if the core

radius is smaller than the Hill radius; otherwise, the clump is tidally limited and accretion is suppressed. Further reduction of the Hill radius would cause the clump to be tidally disrupted.

4.3. Clump Migration

In most of our fragmentation cases, the clumps migrate inward roughly on the type I timescale initially, given by the expression (Tanaka et al. 2002)

$$\tau_{\rm mig} = \frac{R}{\dot{R}} = \frac{h^2}{4Cq\mu}\frac{2\pi}{\Omega}, \quad (16)$$

where $C = 3.2 + 1.468\xi$, ξ is the slope of the surface density $\Sigma \propto r^{-\xi}$, $h = H/R$, $\mu = \pi\Sigma(R)R^2/M_*$, and $q = M_c/M_*$, where M_c is the clump mass. With our disk parameters, this becomes

$$\tau_{\rm mig} = 784\left(\frac{M_c}{0.01M_\odot}\right)^{-1}\left(\frac{R}{100\,{\rm AU}}\right)^{1.75}{\rm yr}. \quad (17)$$

Our simulations confirm this timescale estimate early in the simulations shortly after clump formation, as shown in the right panels of Figure 8 (the smooth solid curve is from Equation (17)). This is consistent with recent papers on the same subject by Baruteau et al. (2011) and Michael et al. (2011). The upper solid lines in these panels are the migration trajectories followed by the clumps in the simulations, and the spikes are a stochastic component due to the interaction between the clumps and the spiral arms (and sometimes other clumps). Our simulations, however, suggest that as the clump mass increases due to accretion, the migration deviates from the typical type I migration timescale given by Equation (17). This appears to occur because the mass of the clump begins to approach the local disk mass, such that the inertia of the clump plays a role in slowing the migration rate. The type I migration timescale given by Equation (17) is obtained using a linear theory that assumes the underlying disk structure is unperturbed by the clump. Although the clumps are not able to clear gaps in the disk because of the large effective viscosity, the disk response to the clump gravity is nonlinear because the clump Hill radii exceed the local disk scale height. We find that the clump migration rates can be reasonably well fit by the following expression that accounts for the slowing of migration because of the clump inertia

$$\tau_{\rm mig,\,fit} = \tau_{\rm mig}\left(1 + \left(\frac{M_c}{2R^2\Sigma(R)}\right)^2\right). \quad (18)$$

Fits obtained using the above expression are shown by dashed lines in the right panels of Figure 8.

The clump represented by the black curve shown in the upper panel of Figure 8 (run R100_3e-5) slows down its migration when it reaches ~50 AU since it is massive enough (~0.3 $M_\odot$) to open a gap in the disk (see the discussion in Section 5.1).

4.4. Clump Mass

The clumps accrete mass from the disk during their migration as discussed in Section 4.2. There are several characteristic masses that mark transitions from differing types of evolution, as discussed further in Section 5.

The mass limits of clumps in disks undergoing GI can be estimated analytically and compared with our simulation results. The initial clump mass can be estimated as the mass contained in the disk patch whose length scale is equal to that of the most unstable mode (wavelength $\lambda = 2c_s^2/G\Sigma$ with $Q = 1$). Thus,

$$M_{c,\,\rm ini} = \pi(\lambda/2)^2\Sigma(R) = \frac{\pi c_s^4}{G^2\Sigma(R)} = \frac{\pi H^4}{R^4}\frac{M_*^2}{R^2\Sigma}. \quad (19)$$

In our disk setup, $M_{c,\rm ini} = 4.7\times10^{-4}\,M_*(R/{\rm AU})^{0.75}$ (the lower dotted curve in the upper left panel of Figures 9, 10, and 11). When the clump first forms from the breakup of a spiral arm, its shape is elongated due to tidal forces from both the star and the rest of spiral arm. This elongation together with the shock structure along the spiral arms makes the real initial clump mass different from that estimated above.

When the clumps are identifiable and become quasi-spherical, separating from the spiral arms, we found they are close to that which would be implied by Equation (19). But some clumps are a factor of two less massive (e.g., the upper left panel of Figure 10).[6] This is slightly higher than more detailed clump mass calculations and simulations by Boley et al. (2010), suggesting that the initial clump mass can be a factor of several smaller than that estimated using Equation (19). Our initial clumps are $\gtrsim$10 M_J, larger than that found by Boley et al. (2010) and Hayfield et al. (2011). We attribute this to the strong irradiation in our disks requiring larger disk masses before fragmentation can arise.

After a clump collapses, its size is smaller than its Hill radius, enabling it to accrete from the disk during its orbit around the central star (as discussed in Section 4.2). If the clump accretes all the mass along its orbit, the maximum clump mass can be calculated by considering its "isolation mass," defined to be the mass contained in an annulus centered on the orbital radius with half-width equal to the clump Hill radius (e.g., Lissauer 1987; Rafikov 2001):

$$r_H = \left(\frac{M_c}{3M_*}\right)^{1/3}R \sim \left(\frac{4\pi Rr_H\Sigma(R)}{3M_*}\right)^{1/3}R, \quad (20)$$

and

$$M_{c,\,\rm iso} = 4\pi Rr_H\Sigma(R) = \frac{(4\pi\Sigma)^{3/2}R^3}{(3M_*)^{1/2}} = M_*\left(\frac{64H^3}{3R^3Q^3}\right)^{1/2}. \quad (21)$$

With our disk parameters, $M_{c,\rm iso} = 0.023\,M_*(R/{\rm AU})^{0.375}$. This isolation mass is plotted as the upper dotted line in the upper left panel of Figures 9, 10, and 11. It should be noted that this mass is derived assuming that the clump does not migrate during accretion. In reality, the clump migrates and is therefore able to grow to a mass that is larger than the isolation mass.

In our simulations, the surviving clumps start at a mass smaller than the mass estimated by Equation (19) but quickly accrete to the isolation mass. This high accretion rate, and the resulting formation of massive clumps, provides a different picture of clump evolution than the analytic calculations of Nayakshin (2010a), where accretion onto the clump was neglected.

5. CLUMP FATES

Due to the stochastic nature of the migration and accretion, and the different environments in which they form, the clumps

[6] We want to point out that these initial clumps were identified by eye, and when we are certain they are gravitationally bound; the clumps may be less massive when they initially become bound objects.

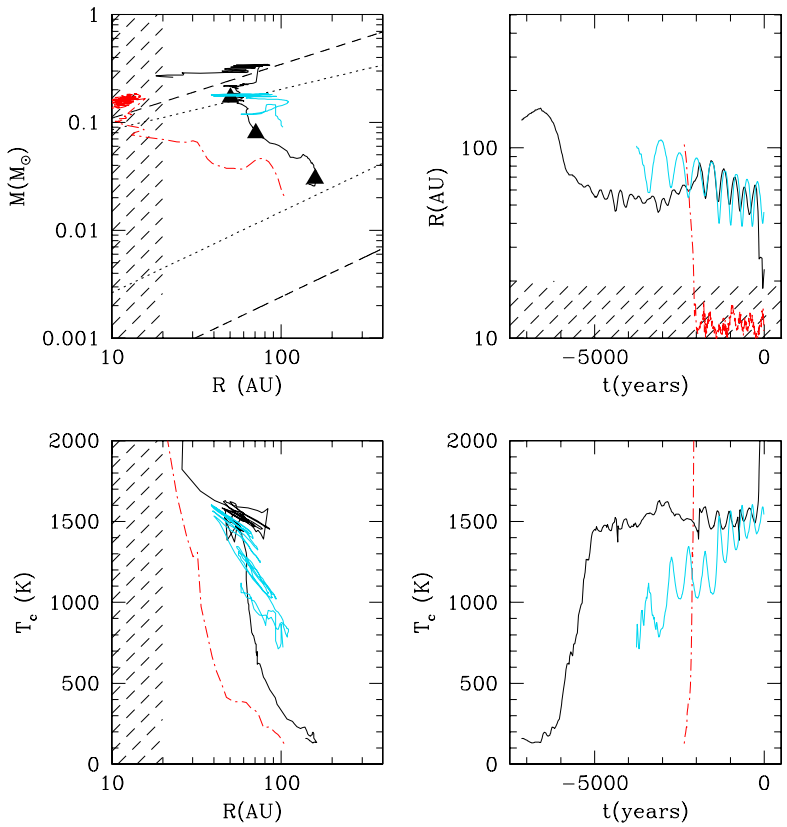

Figure 9. Left: clump masses and central temperatures as a function of position for cases when a gap is opened and migration stops (different colors correspond to different cases in Table 1, and the clump names are given in Table 2). The dotted lines represent the isolation mass (Equation (21)) and minimum clump masses (Equation (19)), while the dashed lines represent the gap-opening masses (Equation (22)). When the clump is close to the inner boundary, its evolution is significantly affected by the inner boundary. Thus, we shade the region where the clump evolution may not be reliable. The three triangles label when the clump mass is 0.03, 0.08, and 0.17 $M_\odot$. The disk surface densities at these three times are shown in Figure 12. Right: the clump radial position in the disk (distance to the star) and the central temperature evolution with time for these cases. The black curve is for the R100_3e-5 case, the cyan curve is for the R200_1e-5 case, and the red curve is for the R65_1e-4 case.

(A color version of this figure is available in the online journal.)

Table 2
Clump Fates

Gap Opening	Tidal Destruction	Across Inner Boundary
[a] A, C, G	E, F, I, J	A[b], B, D, E[c], H, K
3	4	6

Notes.
[a] The clump label corresponds to the clump label in the last column of Table 1.
[b] This clump opens a gap within twice the disk inner radius. The gap opening may be due to the inner boundary condition. Thus we count this case as both crossing the inner boundary and gap opening.
[c] This clump is tidally destroyed within twice the disk inner radius. This tidal destruction may be due to the inner boundary condition. Thus, we count this case as both crossing the inner boundary and as being tidally destroyed.

have different fates in our simulations. In this paper, we have only traced the clumps in the marginal fragmentation cases, where one or two clumps coexist in the disk. When multiple clumps form, clump–clump interaction becomes significant and examination of this is left for a future study. A total of 13 clumps are generated in the marginally fragmenting cases (summarized in the last column of Tables 1 and 2). Of these, three clumps open gaps and stop migrating (as shown in Figure 9), four clumps are tidally destroyed during their migration (three are shown in Figure 10), and six clumps migrate across the inner boundary (three are shown in Figure 11).

5.1. Gap Opening

Figure 9 shows the evolution of the clumps that open gaps and almost stop migration in the disks at the end of our simulations. Results are taken from the simulations R65_1e-4, R100_3e-5, and R200_1e-5 listed in Table 1. In the R100_3e-5 case (black curves), we can see the trend that the clump's inward migration slows down when it opens a gap at ∼50 AU. The change in surface density during gap formation is shown in Figure 12. Two conditions need to be satisfied for gap opening in a non-self-gravitating disk. The first condition is that the Hill radius of the clump needs to be larger than the disk scale height. Using Equation (19), it can be shown that this condition is met when the clump mass M_c is smaller than the initial clump mass calculated from Equation (19) by a factor of 12 (the lower dashed line in the upper left panel of Figures 9, 10, and 11). Thus, this condition is satisfied almost all the time considering that the initial clump is only a few times less massive than the mass given by Equation (19). The second condition is that $M_c/M_* > 40/R_e$ (Lin & Papaloizou 1979) where the effective Reynolds number at the clump location is $R_e = Rv_k/\alpha H c_s$. Here, v_k is the Keplerian velocity. For gap opening to occur, the clump mass must satisfy the relation

$$M_{c,\,\mathrm{gap}} > 40 M_* \frac{\alpha H^2}{R^2}. \quad (22)$$

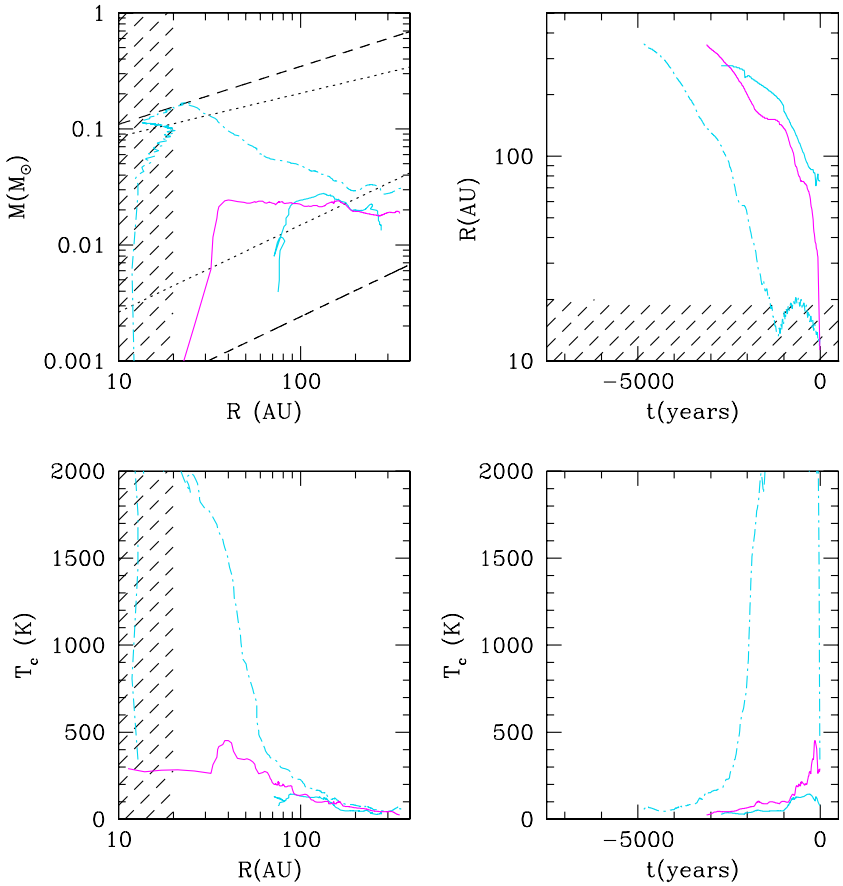

Figure 10. Same as Figure 9 but for cases when tidal destruction occurs. These clumps correspond to the clumps labeled in Tables 1 and 2. The cyan curves are for the R200_1e-5 case, and the magenta curve is for the R200_3e-6noirr case.
(A color version of this figure is available in the online journal.)

With the irradiation temperature we adopted, $H/R \sim 0.029\,(R/\mathrm{AU})^{0.25}$, and $M_{\mathrm{c,gap}} > 0.034\,\alpha\,M_*(R/\mathrm{AU})^{0.5}$. Since α can be as large as 1 (see Section 6.1), the gap-opening value of M_c is shown as the upper dashed line in the upper left panels of Figures 9, 10, and 11.[7] Figure 9 shows clearly that when the clump mass is above this line, the migration slows down significantly. The gap opening is illustrated further in Figure 12, and the gap forms when the clump mass $M_c \sim 0.17\,M_\odot$, corresponding to the point where the clump is close to the critical mass in Equation (22) and stops migrating. Numerous previous studies have showed that even in the presence of a gap, gas can accrete onto the gap forming object by diffusion of gas through the gap (e.g., Bryden et al. 1999; Kley 1999; Nelson et al. 2000). It is for this reason that some of the clump masses are able to grow beyond the gap forming mass in Figure 9.

For the black curve in the top right panel of Figure 9, the clump appears to migrate inward sharply at the end of the simulation. By investigating this inward migration in detail, we found that another clump forms at the edge of the gap, and the interaction between these two clumps leads to this inward migration.[8] This clump formation at the gap edge in the GI disk could be due to the edge instability studied by Lin & Papaloizou (2011a). We also notice that the clump represented by the black curve in Figure 9 migrates slightly outwards after gap opening, which is similar to the finding by Lin & Papaloizou (2011b) due to the clump's interaction with the edge instability. But the final fate of the clump is quite uncertain due to the interactions between clumps, GI spiral arms, and the edge modes.

5.2. Tidal Destruction

Out of 13 clumps in our simulations, 4 are tidally destroyed during their migration, as illustrated by the upper left panel of Figure 10. These cases support the clump tidal destruction picture suggested by Boley et al. (2010), Nayakshin (2010a, 2010b, 2011), and Vorobyov (2011). As pointed out by these papers, since the condition within the clump can be very different from the disk, different chemistry and solid processing are expected. If the core can be tidally destroyed, the products can be released back into the protoplanetary disk, affecting planet formation. The process of tidal destruction is shown in Figure 13. Starting from the upper left panel, the clump is initially well within its Hill sphere. When the clump migrates inward, its Hill radius decreases until it approaches the clump radius (upper right panel). At this stage, due to the strong tidal force, the clump is elongated along the radial direction (lower left panel). The clump is continuously stretched and loses mass when it migrates further inward, and finally it dissolves into the spiral arm.

Whether or not the clump is tidally disrupted depends on the competition between cooling/shrinking and migration. If

[7] The real gap-opening mass can be slightly smaller than that shown in these figures since we assume the maximum $\alpha = 1$ in these plots.
[8] The interaction between these two clumps can be seen in the upper right panel of Figure 9 where there are periodic oscillation for the clump's position in the disk as soon as the second clump forms in the disk. The oscillation in the cyan curve is also due to the interaction with another clump in the disk.

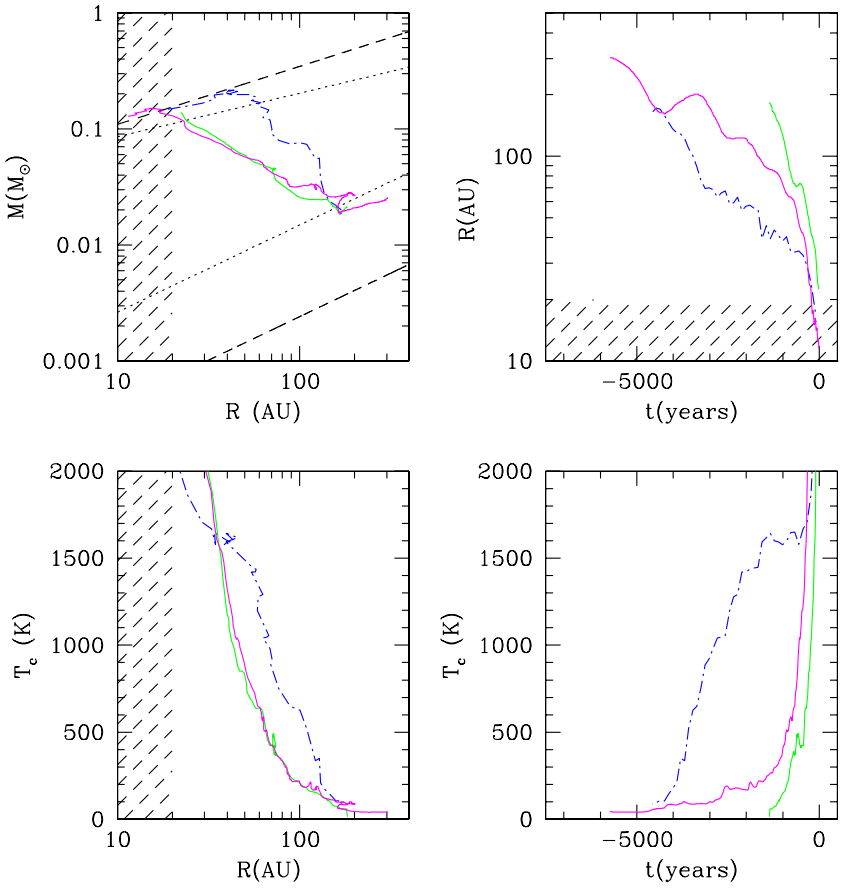

Figure 11. Same as Figure 9 but for cases when the clumps migrate to the inner boundary. These clumps correspond to the clumps labeled in Tables 1 and 2. The magenta curve is for the R200_3e-6noirr case, the green curve is for the R100_1e-5I case, and the blue curve is for the R100_1e-4 case.
(A color version of this figure is available in the online journal.)

the migration is fast, and the clump radius becomes larger than its Hill radius ($r_c > r_H$), the clump will be tidally destroyed. Assuming $r_c \sim r_H$ when the clump first forms, this condition becomes

$$-\dot{r_c} < -\dot{r_H} = -\frac{r_H \dot{M}_c}{3M_c} - \frac{r_H \dot{R}}{R} \tag{23}$$

or

$$\tau_{\rm cool} > \frac{\tau_{\rm mig}}{-3\tau_{\rm mig}/\tau_{\rm acc} + 1}, \tag{24}$$

where $\tau_{\rm cool} = -r_c/\dot{r_c}$ due to cooling, $\tau_{\rm acc} = M_c/\dot{M}_c$, and $\tau_{\rm mig} = -R/\dot{R}$, if $r_c \sim r_H$. The left side is the cooling timescale, while the right side is a combination of the accretion and migration timescales. As shown above, although the migration and cooling timescales are important, rapid accretion prevents the clump's tidal destruction since increasing clump mass increases the Hill radius. The cooling timescale is given by Equation (47) below as

$$\tau_{\rm cool,\,r} = 104 \left(\frac{r_c}{10\,{\rm AU}}\right)^{-2.5} \left(\frac{M_c}{0.01 M_\odot}\right)^{0.5} {\rm yr} \tag{25}$$

if the clump/core is radiative with the polytrope we assumed (see Appendix C), and

$$\tau_{\rm cool,\,c} = 122 \left(\frac{r_c}{10\,{\rm AU}}\right)^{-1.8} {\rm yr}, \tag{26}$$

if the clump is convective. During the clump accretion and contraction, this timescale gets significant larger with time. On

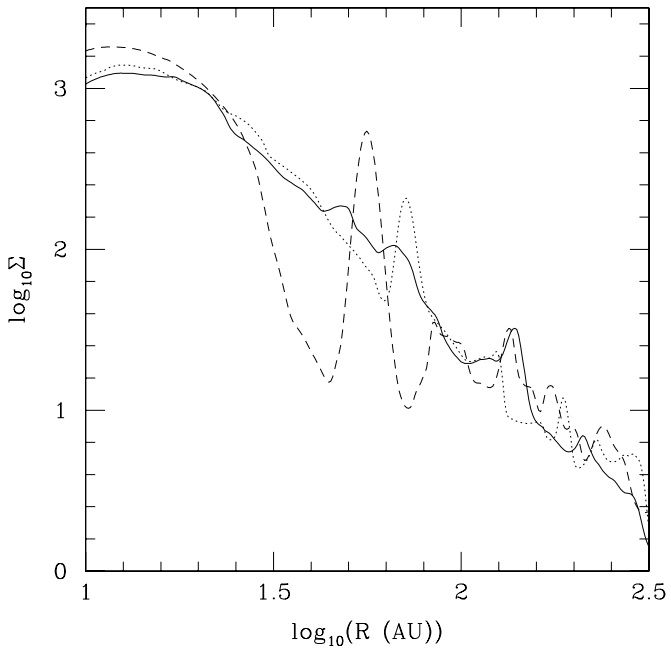

Figure 12. Disk azimuthal averaged surface density for the R100_3em5 case when the clump mass is 0.03 $M_\odot$ (solid curve), 0.08 $M_\odot$ (dotted curve), and 0.17 $M_\odot$ (dashed curve). As clearly shown, the clump stops its migration (corresponding to mass 0.17 $M_\odot$ in Figure 9) when a gap forms.

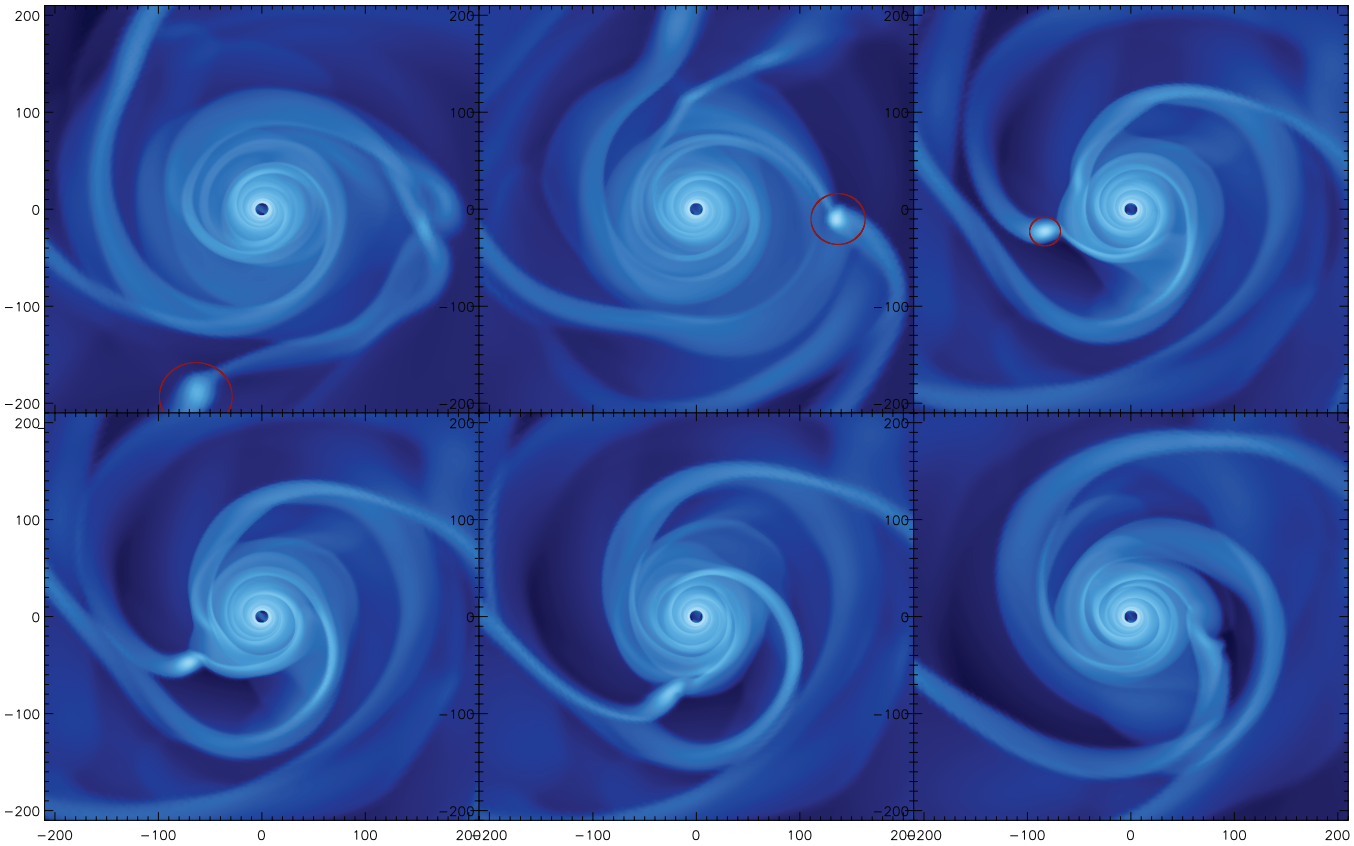

Figure 13. Clump formation, migration, and tidal destruction for the R200_1e-5 case. From left to right and top to bottom, setting the first image at time $t = 0$, the time slots for subsequent images are 546 yr, 1067 yr, 1103 yr, 1174 yr, and 1328 yr.

(A color version of this figure is available in the online journal.)

the other hand, with Equation (14), the accretion timescale is

$$\tau_{\rm acc} = \frac{2M}{3\Sigma\Omega(1.7R_H)^2} = 1112\left(\frac{M}{0.01M_\odot}\right)^{1/3}\left(\frac{R}{100\,{\rm AU}}\right)^{1.25}{\rm yr}. \quad (27)$$

The migration timescale from Equation (17) is

$$\tau_{\rm mig} = 784\left(\frac{M_c}{0.01M_\odot}\right)^{-1}\left(\frac{R}{100\,{\rm AU}}\right)^{1.75}{\rm yr}. \quad (28)$$

Since these three timescales are close to each other, it is natural that the clumps may have different fates due to the stochastic migration and accretion. Equation (24) above suggests that rapid migration combined with slow accretion can lead to clump tidal destruction. As shown in Figure 14, two similar clumps can form at the same time, but the one that undergoes rapid migration is tidally destroyed, while the one that has a longer time to cool and shrink survives. Rapid migration also limits a clump's ability to accrete, since it is unable to cool and contract during the migration, and ends up more or less filling its Hill (Roche) sphere. In the extreme cases, this leads to tidal disruption as described above.

5.3. Migration to the Inner Boundary

Although 6 out of 13 clumps migrate through the inner boundary without gap opening and tidal destruction, this is simply because we adopt an inner boundary that is located at ∼2.5–10 AU, so the ultimate fate of these clumps is not known. Some illustrative cases are shown in Figure 11, and are described in Table 1. There is one gap-opening case and one tidal destruction case occurring close to 10 AU, as shown in Figures 9 and 10, showing that both gap opening and tidal destruction can occur at small radii. With a smaller inner boundary, we would clearly expect more clumps to open gaps or be tidally destroyed as they migrate into the inner disk. It is unclear if any clump can survive migration all the way to the central star. The naive timescale arguments given above seem to suggest that the clump may be subject to tidal destruction at smaller radii due to the fact that the migration timescale decreases significantly at smaller radii with bigger clump mass (M_c^{-1}), while the cooling timescale increases with bigger clump mass ($M_c^{0.5}$ or independent of clump mass). We note that when the clump mass exceeds the local disk mass the migration slows down, and the migration time increases with clump mass as indicated by Equation (18). Also, because the clump central temperature is almost always above 1500 K when it migrates to the inner disk (see the bottom panels in Figures 9, 10, and 11), the clump becomes dynamically unstable and should collapse to form a second core (subject to overcoming the angular momentum barrier provided by its spin). It will shrink considerably, leaving the final fate of the clump unclear. Further accretion may lead to gap formation and slowed migration, increasing the survival probability of the clump.

From a statistical point of view, however, we might expect a fragmenting disk to form a binary or multiple star system. If a

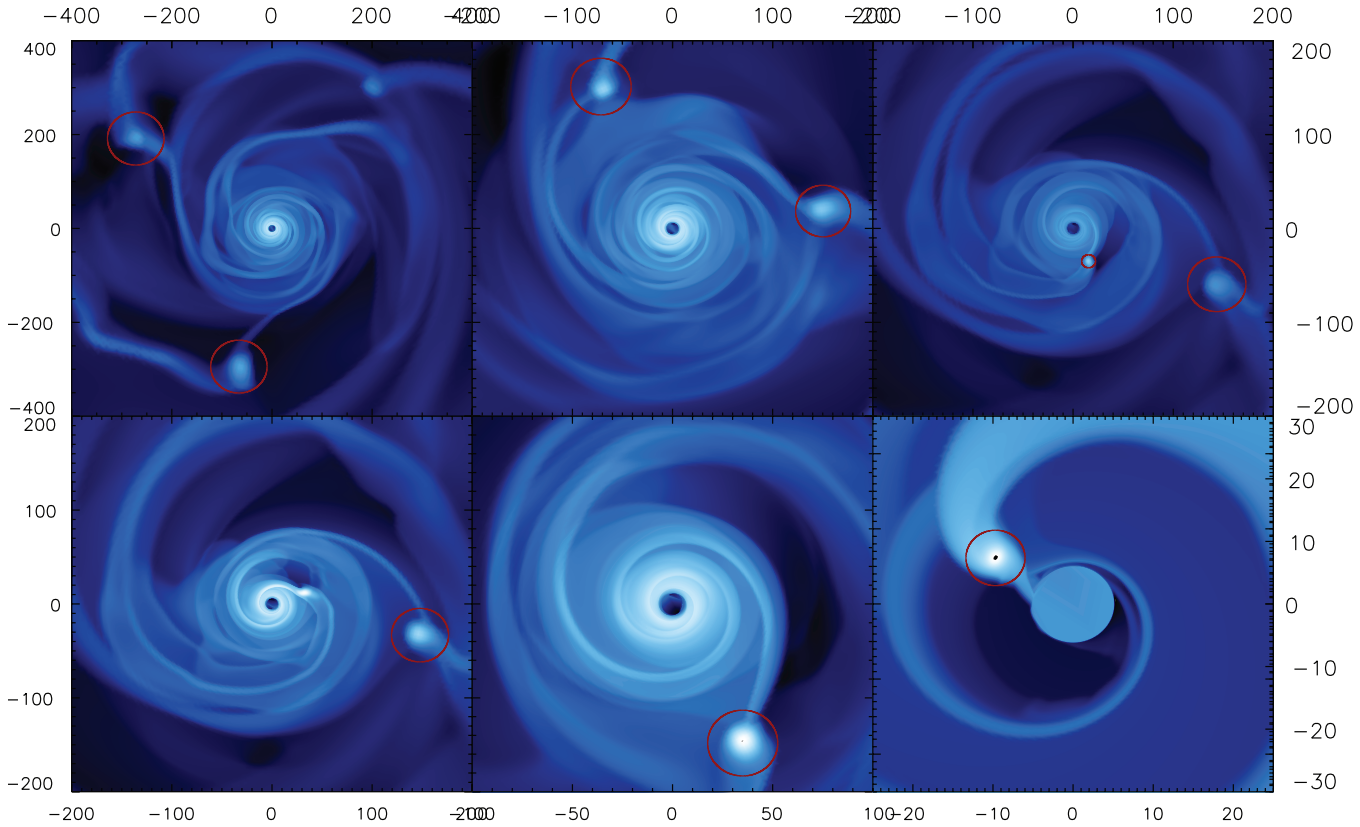

Figure 14. Two clumps forming at the same time but with different fates for the R200_3e-6noirr case. From left to right and top to bottom, setting the first image at time $t = 0$, the time slots for subsequent images are 1660 yr, 3036 yr, 3084 yr, 4898 yr, and 6072 yr.

(A color version of this figure is available in the online journal.)

less massive clump is tidally destroyed or migrates to the central star, a new clump can still form in the outer disk and migrate inward. If one clump forms and happens to become massive enough to open a gap, it will stay there and survive to form a binary companion. The common occurrence of close binary star systems indicates that inward migration of clumps cannot always lead to tidal disruption.

6. FRAGMENTATION AND CLUMP EVOLUTION: ANALYTIC MODELS

In this section, we will review analytic estimates for fragmentation radii and develop a simple model for clump evolution. By comparing the numerical results with the analytic estimates, we can constrain some fundamental parameters in the analytic model (e.g., we will constrain the critical α for the disk fragmentation) and study the roles played by different physical processes.

6.1. Analytic Estimates for Fragmentation

The parameter space for GI-induced disk fragmentation has been explored analytically by several authors (Rafikov 2005, 2007, 2010; Levin 2007; Kratter et al. 2008, 2010a; Cossins et al. 2010; Zhu et al. 2010a). The derivations are summarized in Appendix D.

Analytic estimates for the critical radius of fragmentation as a function of the mass infall rate are shown as curves in Figure 2 with $\alpha_c = 0.06$ or 1, where α_c is the critical fragmentation viscosity parameter. When the equivalent viscosity parameter of the gravitationally unstable disk is larger than α_c, the disk will fragment. Rice et al. (2005) have shown that for non-irradiated disks and a variety of values of specific heat ratios, $\alpha_c \sim 0.06$. Kratter & Murray-Clay (2011) suggested that irradiation may alter the disk fragmentation criterion. Recently, Rice et al. (2011) have done 2D simulations showing that the critical α_c decreases with irradiation.

However, this α_c was derived by assuming the disk cools at a multiple of the orbital timescale throughout fragmentation. With realistic radiative cooling this may not be the case because of the trapping of radiative energy, as discussed later.

The trend of these curves can be understood under two limits: the disk temperature is dominated by viscous heating due to the GI, or it is irradiation dominated. In the viscous heating-dominated limit, the fragmentation radius $R_f \propto \alpha_c^{0.3} \dot{M}^{-0.07} M_*^{1/3} \kappa_R^{2/9}$ (see Equation (D9)). Thus, R_f has a very weak dependence on $\dot{M}$. This is shown in Figure 2 where R_f is almost vertical at ~50 AU when the disk accretion rate is high. On the other hand, if the opacity depletes by a factor of 1000 (κ_R is 0.1% of the nominal value), R_f decreases by a factor of 5 to ~10 AU.

In the irradiation-dominated limit, $R_f \propto (\dot{M}/\alpha_c)^{-4/3} M_*^{1.95}$ (see Equation (D12)). Thus, R_f depends sensitively on $\dot{M}$ as shown in Figure 2, but is independent of the opacity. On the other hand, in the envelope irradiation-dominated limit (assuming $T_{\rm irr} = $ const), the disk will fragment everywhere as long as $\dot{M} > 2c_{s,\,\rm irr}^3 \alpha_c / G$ ($Q \sim 1.5$ is assumed, corresponding to the horizontal dotted line in Figure 2), below which the disk will not fragment at any radius.

Furthermore, as shown in Figure 2, R_f is very sensitive to the value of α_c in the irradiation-dominated case ($R_f \propto \alpha_c^{4/3}$)

although it is less sensitive in the viscous heating-dominated case ($R_f \propto \alpha_c^{0.3}$).

Figure 2 shows that the analytic estimate agrees with simulations reasonably well. But it also suggests that α_c is somewhat larger than 0.06, especially at low infall rates. We think this discrepancy is caused by the following.

1. We assume the infall rates equal the disk accretion rates in Equation (D3) and Figure 2. In reality, in order to conserve angular momentum, some of the infall mass will be transported outward, so the net inward mass flux will be smaller than the infall rate. We estimate that all points in Figure 2 should shift down by $\lesssim$0.2 in the logarithmic scale if the vertical axis is the disk accretion rate.
2. With irradiation, the disk is gradually built up from a gravitationally stable state to an unstable state by infall. This gradual buildup toward GI leads to a transient marginal state which avoids the strong density fluctuations that arise from an initially massive unstable disk as considered in most previous simulations. The gradual buildup of the GI in our simulations makes the disk less likely to fragment. This mechanism is similar to that discussed by Clarke et al. (2007), who showed that, compared with the cases starting with rapid cooling, gradually increasing the cooling rate suppresses fragmentation.
3. With realistic cooling instead of orbital cooling, radiative trapping makes gravitationally bound clumps harder to cool during their collapse, suppressing disk fragmentation. For example, the cooling time is defined as the ratio of the thermal energy of the clump, E, to the clump luminosity, L_c, which is given by

$$L_c = \frac{4\pi r_c^2 \sigma T_c^4}{\kappa \Sigma_c}. \quad (29)$$

If we assume $\kappa = \kappa_0 T^a$, and $\Sigma_c r_c^2 \sim M_c$, we have

$$\tau_{\rm cool} \sim \frac{M_c^2 c_V \kappa_0}{4\pi r_c^4 \sigma T_c^{3-a}}, \quad (30)$$

where c_V is the specific heat capacity. If we assume $T_c r_c$ is constant ($r_0 T_0$), the above equation is

$$\tau_{\rm cool} = \frac{M_c^2 C_V \kappa_0 T_c^{1+a}}{4\pi r_0^4 T_0^4 \sigma}. \quad (31)$$

Since $a = 1.5$, $t_{\rm cool} \propto T^{2.5}$ (a more quantitative estimate is given in Equation (47)). As the clump collapses and heats up, the cooling time gets longer. Clumps with realistic cooling have longer cooling times than clumps undergoing constant orbital cooling in previous simulations used to determine α_c. We need a smaller $t_{\rm cool}$ (than that used in the constant orbital prescription) to start with for the clump to continue to collapse. This implies, because $\alpha \propto 1/t_{\rm cool}$, a larger equivalent α_c in the analytic fragmentation estimate.

Finally, note that even if α_c is the same in the irradiation-dominated cases as the viscous-dominated cases, irradiation still suppresses disk fragmentation (as shown by the flattening of the critical R in the irradiation-dominated regime in Equation (D3)). This is simply due to irradiation setting a minimum disk temperature, so that the disk needs to be hotter to cool. With the higher internal energy and longer cooling time, irradiated disks are harder to fragment. From the disk accretion point of view, even with the same α_c, irradiated disks have larger temperature so that the kinematic viscosity ν (which is $\propto T$) is larger and thus the critical accretion rate is higher.[9]

6.2. Analytic Models of Clump Evolution

Although our simulations are 2D, we can construct simple analytic models to study the clump evolution by assuming the clump is spherical. In the following, we will calculate clump evolution using models of hydrostatic self-gravitating gaseous spheres to represent the first core of the clump, and follow the birthline calculations as in protostar formation but with migration and accretion considered.

The dynamical timescale for clump collapse is much shorter than its Kelvin–Helmholtz (cooling) timescale (Nayakshin 2010a). Thus, we can assume the clump is in quasi-hydrostatic equilibrium (the first core) before its central temperature reaches $\sim$1500 K when dust sublimates and the opacity drops suddenly (Section 4.1). Whether the first core is convectively stable seems to depend on its density, and remains a matter of debate (Wuchterl 1993; Nayakshin 2010a). In the following we will discuss both cases. We want to point out that our radiative core has a polytropic index, n_e (different from the gas adiabatic index), equal to 1.5 and the convective core has a polytropic index equal to 2.5 (see Appendix C). Boley et al. (2010) have found that a polytrope with index 2.5 fits Helled & Bodenheimer (2010) data very well, which is not surprising considering their core is convective. Note that for the gaseous first cores we are discussing here, polytropic indices running between 1.5 and 2.5 cover a wide parameter space.[10]

As derived from Equation (C2) in Appendix C, the luminosity is given by

$$L_{c,r} = \frac{64\pi\sigma}{3\kappa_0}\left(\frac{G\mu}{\Re}\right)^{2.5}\frac{0.424^{1.5} M_c^{1.5}}{2.5 r_c^{-1.5}} \quad (32)$$

for a radiative core, and by

$$L_{c,c} = 4\pi\sigma\,(20.48\kappa_0)^{-4/5}\left(\frac{G\mu}{\Re}\right)^{14/5} r_c^{4/5} M_c^2 \quad (33)$$

for a convective core (Equation (C19)).

With our opacity this can be reduced to

$$L_{c,r} = 2\times10^{-3} L_\odot \left(\frac{M_c}{0.01 M_\odot}\frac{r_c}{10\,\rm AU}\right)^{1.5} \quad (34)$$

and (Equation (C20))

$$L_{c,c} = 1.715\times10^{-3}\,L_\odot \left(\frac{M_c}{0.01\,M_\odot}\right)^2 \left(\frac{r_c}{10\,\rm AU}\right)^{0.8}. \quad (35)$$

[9] The α description for GI assumes locality of the GI (see Equations (D1) and (D2)), which has been studied by Cossins et al. (2009). They have shown that the pattern speed of spiral arms in GI disks roughly equals the disk local Keplerian speed, so that the anomalous term of the energy transport in GI disks is negligible. On the other hand, Cossins et al. (2009) and Forgan et al. (2009) pointed out that with increasingly larger disk masses, the assumption of local energy deposition gradually breaks down since lower mode spiral arms become strong. Irradiated disks are normally massive, so our argument is not exact and only acts as a guide.

[10] A polytrope with index 1.5 can also represent the structure of a convective core for a monatomic ideal gas sphere with dust opacity having temperature dependence power $a = 1.5$ ($n_e = 3 - a$).

Thus, the effective temperature is

$$T_{\rm eff,\,r} = \left(\frac{L}{4\pi r_c^2\sigma}\right)^{0.25} = 26\,{\rm K}\left(\frac{M_c}{0.01M_\odot}\right)^{0.375}\left(\frac{r_c}{10\,{\rm AU}}\right)^{-0.125} \quad (36)$$

and

$$T_{\rm eff,\,c} = \left(\frac{L}{4\pi r_c^2\sigma}\right)^{0.25} = 25\,{\rm K}\left(\frac{M_c}{0.01M_\odot}\right)^{0.5}\left(\frac{r_c}{10\,{\rm AU}}\right)^{-0.3}. \quad (37)$$

The clump central temperature is then (Equations (C4) and (C8))

$$T_{c,\,r} = 138\,{\rm K}\left(\frac{M_c}{0.01M_\odot}\right)\left(\frac{r_c}{10\,{\rm AU}}\right)^{-1}, \quad (38)$$

$$T_{c,c} = 179\,{\rm K}\left(\frac{M_c}{0.01M_\odot}\right)\left(\frac{r_c}{10\,{\rm AU}}\right)^{-1}. \quad (39)$$

The clump loses energy through radiation and shrinks. Thus, an energy equation is required to derive the clump's evolution. The approach we will take is quite similar to the protostellar birthline calculations by Hartmann et al. (1997), but instead of considering energy conservation, we consider the conservation of the Jacobi-like energy integral (Γ) in a frame corotating with the clump. We have

$$\Gamma = \int d^3x\rho\left(\frac{1}{2}v^2 + u + w + \phi_T\right), \quad (40)$$

where $\phi_T = -(3/2)\Omega^2x^2$ is the tidal expansion of the effective potential about the clump, u is the internal energy per unit mass, and w is the potential energy per unit mass. Compared with the total energy calculated by

$$E = \int d^3x\rho\left(\frac{1}{2}v^2 + u + w\right) = K + U + W, \quad (41)$$

an additional energy due to the tidal potential is present. In the picture of the clump accretion, each of these terms sensitively depends on flow structure around the clump, which is uncertain. First, due to the tidal force, the accretion flow from the outside of the Hill sphere onto the clump does not conserve angular momentum with respect to the clump unless a special flow geometry is met.[11] Thus, the structure within the Hill sphere cannot be determined by rigorous analytical arguments. Second, even if the angular momentum is approximately conserved close to the clump and far inside the Hill sphere, additional angular momentum transport mechanism (e.g., magnetorotational instability (MRI)) and the boundary layer physics may be important. For example, if angular momentum within the Hill sphere is weak, it is likely to form a rotationally supported giant clump. On the other hand, if it is like a mini-"protostellar system," the clump is compact and slowly rotating.

For the most simple case, first we study the non-rotating hydrostatic core with a polytrope structure having the polytropic index n_e, which has the following gravitational and internal energy:

$$E = U + W = -\left(1 - \frac{1}{3(\gamma-1)}\right)\frac{3}{5-n_e}\frac{GM_c^2}{r_c}. \quad (42)$$

[11] In a shearing sheet approximation, the flow needs to be symmetric/axisymmetric in the R direction to conserve angular momentum.

With $\gamma = 7/5$ for diatomic gas,

$$E = -\frac{0.5}{5-n_e}\frac{GM_c^2}{r_c}. \quad (43)$$

Consider Δm amount of gas is added to the clump, with the total energy

$$\Delta E = -\varpi\frac{GM_c\Delta m}{r_c}, \quad (44)$$

where ϖ represents the coefficient by adding all the factors from gravitational energy, thermal energy, and the kinetic energy brought by the accreted mass (Prialnik & Livio 1985). For a cold accretion flow which is in Keplerian rotation around the clump $\varpi = 0.5$, while for an accretion disk with boundary layer, $\varpi = 1$. Then, the star adjusts to a new polytropic configuration with mass $M_c+\Delta m$ and radius $r_c + \Delta r_c$. During the time interval Δt of mass addition, the conservation of the Jacobi-like energy L yields

$$L_c\Delta t - \frac{0.5}{5-n_e}\frac{G(M_c+\Delta M_c)^2}{(r_c+\Delta r_c)} = -\frac{0.5}{5-n_e}\frac{GM_c^2}{r_c} - \frac{GM_c\Delta m}{r_c}\varpi - \Delta\phi_T. \quad (45)$$

This reduces to

$$L_c = -\frac{0.5}{5-n_e}\frac{GM_c^2}{r_c^2}\dot{r_c} + \left(\frac{1}{5-n_e} - \varpi\right)\frac{GM_c\dot{M_c}}{r_c} - \dot{\phi_T}. \quad (46)$$

At the Hill radius, ϕ_T is close to the gravitational potential with respect to the clump. Deep in the Hill sphere, ϕ_T is significantly smaller than u. Thus if the clump is very small compared with the Hill sphere, $\dot{\phi_T}$ can be ignored, as we will assume in the following.

As shown in Figure 6, the rotational energy becomes important as the clump accretes a significant amount of disk mass, thus it is quite uncertain what the appropriate value for ϖ is.

If the clump accretion is ignored, the cooling timescale is

$$\tau_{\rm cool,\,r} = \frac{E}{L} = \frac{r_c}{\dot{r_c}} = 102\left(\frac{r_c}{10\,{\rm AU}}\right)^{-2.5}\left(\frac{M_c}{0.01\,M_\odot}\right)^{0.5}{\rm yr}, \quad (47)$$

$$\tau_{\rm cool,\,c} = 122\left(\frac{r_c}{10\,{\rm AU}}\right)^{-1.8}{\rm yr}. \quad (48)$$

In order to form a closed relationship so that we can evolve the clump's properties with time, we have made several simplifications with attendant large uncertainty. The first simplification is to treat the structure of the clump as a polytrope. Whether the clump is radiative or convective changes the polytropic index significantly from ~1.5 to 2.5. To explore this uncertainty, we use both radiative and convective models. The second uncertainty is the accretion physics/boundary layer around the clump. We will explore this by varying ϖ from 0.5 to 1. The third simplification is assuming the clump is non-rotating, which is not necessarily the case as shown in Figure 6. The rotation of the clump can change our analysis significantly, not only because the clump changes shape due to rotation, but also the change of ϕ_T is comparable to u if the clump's radius is comparable to the Hill radius. We do not attempt to explore this uncertainty since there is no simple structure solution for a fast rotating clump. Thus, this remains a significant uncertainty in our analysis, which the reader should keep in mind.

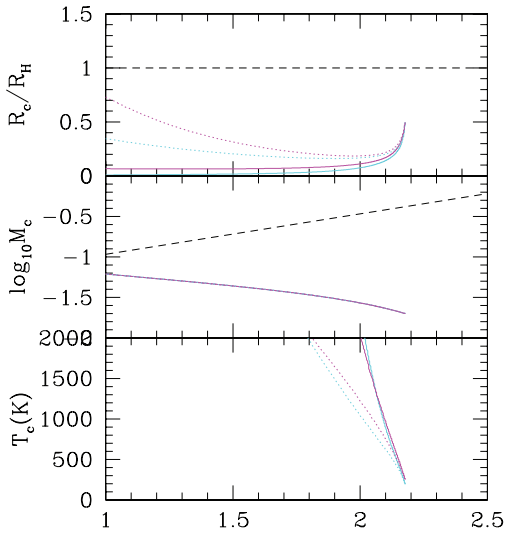

Figure 15. Values of r_c/r_H, mass (in units of $M_\odot$), and central temperature for a clump as a function of its position in the disk for different clump parameters. The purple curves are for the convective cores with $n_e = 2.5$, while the cyan curves are for the radiative cores with $n_e = 1.5$. The solid curves are calculated with $\varpi = 1$, while the dotted curves are calculated with $\varpi = 0.5$. The dashed line in the top panel shows when the tidal destruction happens, and the dashed line in the middle panel shows when the gap opening occurs in the disk.

(A color version of this figure is available in the online journal.)

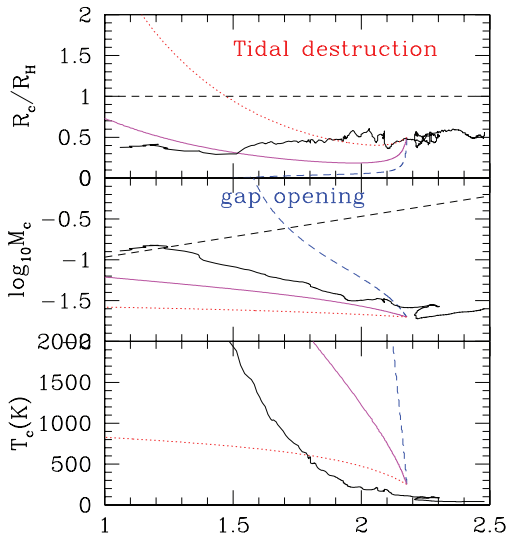

Figure 16. Values of r_c/r_H, mass (in units of $M_\odot$), and central temperature for a clump as a function of its position in the disk. The clump's evolution is from right to left, while it migrates inward. The solid black curve is from our simulation with clump K (shown in Figures 8 and 11). The solid purple curve is from our simple analytic model with a convective core assumption and $\varpi = 0.5$. The dotted red curve is from our analytic model but with five times the nominal migration speed (Equation (18)), and the clump is tidally destroyed, which can be compared with Figure 10. The dashed blue curve is from our analytic model but with 1/5 of the nominal migration speed, and it open gaps in the disk around 30 AU, which can be compared with our simulations in Figure 9. The dashed line in the top panel shows when the tidal destruction happens, and the dashed line in the middle panel shows when the gap opening occurs in the disk.

(A color version of this figure is available in the online journal.)

Equations (15), (32) or (33), (38) or (39), and (46) form a closed model for clump evolution as long as the initial clump properties ($M_c(t = 0)$, $r_c(t = 0)$) are given. At time t, with known $M_c(t)$ and $r_c(t)$, the luminosity, $L(t)$, can be derived from Equation (32). Then $r_c(t + \Delta t)$ can be derived based on $\dot{r_c}$ from Equation (46) with $L(t)$ and $\dot{M}_c$ (Equation (15)). $M_c(t + \Delta t)$ can also be derived with $\dot{M}_c$ from Equation (15). T_c from Equation (38) can be used to derive the opacity and the equation of state. At this point, all the quantities for the clump at time $t + \Delta t$ have been updated. Then with the migration velocity given by Equation (18), the clump's position can be updated. By comparing the clump's core size with its Hill radius (which depends only on the clump's mass and position in the disk), we can determine whether the clump can continue accreting or will be tidally destroyed.

To compare with our simulations, we assume the initial clump at 150 AU has mass $0.02\,M_\odot$ and the clump radius is half its Hill radius, as suggested by the simulation results. Following the above procedure, the clump evolution is shown in Figure 15 with $n_e = 1.5$ or 2.5 and $\varpi = 0.5$ or 1. As shown in the figure, the clump evolution is not sensitive to the structure of the clump (n_e), but very sensitive to accretion onto the clump (ϖ). This is due to the high accretion rate onto the clump, which dominates the energy budget in the energy equation above. In this sense, the interior structure of the clump may affect the clump evolution significantly since a convective core can transport angular momentum outward more easily, making the clump rotate rigidly. Our simple theory predicts a higher central temperature compared with our simulations shown in Figure 11, which could be due to our simple radiative cooling treatment in 2D simulations or the absence of clump rotation in the analytic models.

As discussed in Section 5.2, the interplay between clump cooling, migration, and accretion determines the clump's evolution and fate. Cooling allows the clump to shrink and inhibits tidal destruction, while inward migration reduces the Hill radius and promotes tidal destruction. On the other hand, accretion increases the Hill radius and inhibits tidal destruction. Since these three timescales are comparable, as discussed in Section 5.2, stochastic migration and accretion may lead to different clump fates. To examine the effect of varying parameters in our analytic model, we calculated cases with 1/5 and 5 times the migration speed. As shown clearly in Figure 16, rapid migration leads to tidal destruction around 30 AU. The clump properties here are similar to our simulation results in Figure 10. On the other hand, slower migration allows more time to cool, shrink, and accrete. Eventually, the clump becomes massive enough to open a gap during its migration. Clump properties from our simple model also agree with those from our simulations of gap-opening clumps in Figure 9.

Finally, we want to emphasize that this simple model is highly idealized, and the behavior of r_c depends on the polytropic index, the detailed opacity, and the accretion physics around the clump. But it still provides a useful tool for exploring different evolutionary scenarios, and for comparison with hydrodynamic simulations.

7. DISCUSSION

7.1. Planets and Multiple Star Systems

Recent direct imaging observations have revealed companions around A-type stars (e.g., Fomalhaut, Kalas et al. 2008; HR 8799, Marois et al. 2008). Although fragmentation from GI has been proposed to explain these giant planets, our results pose two potential challenges.

1. *Mass challenge*. Including irradiation, the disk needs to be quite massive to be gravitationally unstable ($M_d > 0.3\,M_\odot$). Although the initial fragments can have masses

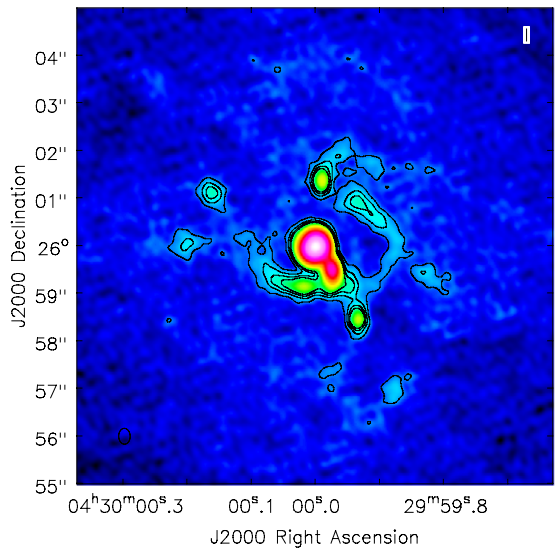

Figure 17. Synthetic ALMA image (with CASA) at 3 mm for the R100_3e-5 case, assuming this disk is in Ophiuchus. The disk effective temperature at 3 mm is approximated with Equation (4) and the central star is assumed to have 5000 K effective temperature. The integration is only 1 minute with Full ALMA (resolution 0.″1). Besides the massive clump close to the central star, several other clumps at ∼100 AU scales are also apparent. The tidally induced spiral arms by the clumps have 5σ detection.

(A color version of this figure is available in the online journal.)

around a few Jupiter masses, they accrete at high rates 10^{-3}–10^{-1} M_J yr^{-1}, so that after only a few thousand years clumps may reach their isolation masses, which are in the brown dwarf or low stellar mass regime.

2. *Migration challenge*. All clumps migrate inward from hundreds of AU to tens of AU over timescales of 10^3 yr, although the migration has a stochastic component due to the interaction with the spiral arms. There are at least two distinct fates for these migrating clumps. The ones reaching gap-opening masses (corresponding to subsolar masses in irradiated disks) slow their migration; less massive clumps migrate in rapidly and are subject to tidal destruction. Generally, only the massive clumps survive in our simulations, suggesting that GI-induced fragmentation is best suited for forming massive brown dwarfs and close binaries rather than gas-giant planets.

If binary systems are formed by GI fragmentation in disks, the spin axis of these two stars should be parallel and perpendicular to the disk plane. Recent observations on Kepler 16 systems have suggested the spin axis of the binary and the planet around them are all closely aligned (Winn et al. 2011), which support the scenario that they are formed in the disk.

The first cores produced by GI-induced fragmentation can be as large as 10 AU when the core is at 100 AU. Its luminosity can be as high as 0.1 $L_\odot$ if the core mass is 0.1 $M_\odot$ or 0.002 $L_\odot$ if the core is 10 M_J (see Equation (34)). With an effective temperature ∼100 K (Equation (36)), these clumps can be easily detected and resolved by ALMA, as illustrated in Figure 17, but they may be rare because they only live for a few thousand years before they collapse to the second core stage.

Boley et al. (2010) and Nayakshin (2011) have proposed that dust can settle and agglomerate within fragmented clumps, forming a solid core at the center. Subsequent tidal disruption of the clump during inward migration may then lead to the removal of the gas envelope, leaving a surviving rocky body in the disk. Our simulations suggest the tidal destruction of the envelope can happen and may not be rare (4 out of 13 cases) if the disk fragments. Whether the solid core can form is beyond the scope of this paper (see Cha & Nayakshin 2011).

Our simulations have several simplifications that require further consideration. First, our disks are subject to mass infall all the time. If the disk fragments while there is no mass replenishment by infall, the clumps at the outer edge of the disk may not necessarily migrate inward; in other words, small fragments formed near the end of infall may have the best chance of survival at large radii.

A second issue is that we have assumed axisymmetric, smooth infall, which may not be the most typical case. Strong non-axisymmetric perturbations in the infalling material can aid fragmentation (Burkert & Bodenheimer 1993). We do not explore such large perturbations in order to develop well-conditioned numerical simulations.

We emphasize that the 2D nature of our simulations, while enabling us to study clump formation and evolution over long timescales, necessarily omits 3D effects which could be important, such as wave propagation in a stratified disk (Ogilvie & Lubow 1999). However, the fragmentation occurs at large radii, where we expect the disk to be more nearly vertically isothermal due to the dominance of irradiation heating. Of more concern is the crude treatment of the radiative cooling for clump evolution, which may differ significantly in 3D. Finally, we have limited the calculations to a constant value of γ, and have not considered possible instabilities related to, for example, molecular hydrogen rotational thermalization or dissociation.

Considering our limitations, a comparison with existing 3D simulations is necessary. Our results are consistent with the findings by Stamatellos & Whitworth (2009a, 2009b) that planetary mass objects are hard to form in GI unstable disks, while brown dwarfs and low mass stellar companions are common. On the other hand, our work focuses on individual clump evolution in disks where only one clump forms, which is complementary to Stamatellos & Whitworth (2009a, 2009b) where they also studied clump-clump interaction. Boley (2009) has done four simulations with similar mass loading as our simulations, two of which (SIMB and SIMD) can be compared with our simulations. SIMB fragments with an infall rate $\dot{M} \sim 10^{-4}$ $M_\odot$ yr^{-1} at 100 AU, which is consistent with our results. And the clump in SIMD accretes from 6 M_J to 11 M_J supporting the clump accretion scenario. Simulations by Kratter et al. (2010a) have shown that the disk fragments when $\alpha > 1$ and the clumps are quite massive. However, they used a piecewise polytropic equation of state. Harsono et al. (2011) suggested that infall has weakened the disk fragmentation; in other words, the critical α for fragmentation is large. This seems to be consistent with our results. But caution has to be made that we put infall manually by adding disk mass and no shear between the infall and the disk has been set up. We also used radiative cooling instead of orbital cooling as Harsono et al. (2011). Hayfield et al. (2011) have found in some cases, that the clumps accrete at rates $\sim 10^{-5}$ $M_\odot$ yr^{-1} and can grow from several Jupiter masses to 40 M_J. This is similar to what we have found in our simulations. But again, our simple equation of state introduces uncertainties in the disk dynamics and the thermal structure of the clumps.

Although theoretically the clump evolution and fate is complicated by the disk infall history, and clump accretion/migration, observations may provide us clues on the formation mechanism for giant planets found at large distances (e.g., Fomalhaut,

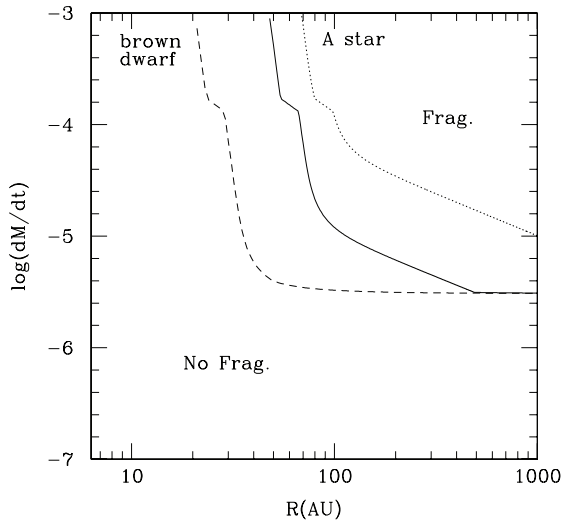

Figure 18. Similar to Figure 2, the fragmentation radii for a typical brown dwarf (0.08 $M_\odot$, 0.01 $L_\odot$) and an A-type star (3 $M_\odot$,100 $L_\odot$) compared with our standard case (1 $M_\odot$, 1 $L_\odot$, solid curve). A $T = 20$ K minimum disk temperature is assumed and $\alpha_c = 1$ has been used.

HR 8799) by measuring the metallicity of these planets (Helled & Bodenheimer 2010, 2011).

7.2. Dependence on Stellar Properties

Figure 18 shows the analytic estimates for the fragmentation radii for disks around brown dwarfs and A-type stars. We chose $M_* = 0.08\,M_\odot$, $L_* = 0.01\,L_\odot$ for the brown dwarf, and $M_* = 3\,M_\odot$, $L_* = 100\,L_\odot$ for the A-type star. The critical fragmentation α_c is 1 and minimum 10 K disk temperature has been applied.

For viscous heating-dominated disks, the fragmentation radius varies from 20 AU (brown dwarf) to 80 AU (A-type star) simply due to $R_f \propto M_*^{1/3}$ in Equation (D9). However, for irradiation-dominated disks, the fragmentation radius varies from 30 AU (brown dwarf) to 1000 AU (A-type star) at $10^{-5}\,M_\odot\,\mathrm{yr}^{-1}$. This sensitive radius dependence for irradiation-dominated disks is due to $R_f \propto L^{1/2}$ in Equation (D11), and the four orders of magnitude variation in luminosity between the A-type star and the brown dwarf. The lowest fragmentation accretion rate is limited by the minimum disk temperature that equals the envelope temperature. This analytic estimate is confirmed by the R200_3e-5L100 case where the disk did not fragment.

We want to emphasize that currently found far away planets (>50 AU) by direct imaging technique are around A-type stars (e.g., HR 8799). Due to the stronger irradiation, the disk needs to be more massive to be gravitationally unstable and the clumps produced by GI can be more massive than our simulation produced. This poses a bigger challenge for GI to explain these giant planets.

These results apply to the formation of fragments for infall in a smooth, non-structured pattern, which probably applies best to the formation of objects of much lower mass than that of the central star. Binary fragmentation can be enhanced by non-axisymmetric infall (Burkert & Bodenheimer 1993; Kratter et al. 2010a), which are likely to dominate the formation of companion stars from turbulent initial conditions.

7.3. Disk Evolution and Outbursts

GI-induced fragmentation has been proposed as a mechanism to explain outbursting protostellar accretion phenomena, as in FU Orionis and Exor objects (Vorobyov & Basu 2005). However, early calculations (Vorobyov & Basu 2005, 2006) used a polytropic equation of state that can artificially enhance fragmentation (Boss 1997; Pickett et al. 2000; Gammie 2001). Recent simulations (Vorobyov & Basu 2010) with an improved energy equation suggest that GI-induced fragmentation only occurs in a fast rotating massive disk with a low background temperature; this is consistent with our results that only infall to large disk radii at high infall rates results in fragmentation. Thus, whether outbursts can be explained by protostellar disk fragmentation sensitively depends on the initial conditions of prestellar cores, which need further observational study.

On the other hand, while Vorobyov & Basu (2005, 2006) argued that the accretion of fragments explain FU Orionis outbursts of accretion from disks, we showed (Zhu et al. 2008, 2009b, 2009c; see also Armitage et al. 2001; Rice et al. 2010) that the GI could trigger bursts of accretion without clumping by thermally triggering the magnetorotational instability (MRI) in the innermost disk. We further analyzed observations to show that the inner ~0.5 AU region of the FU Ori disk during outburst fits the predictions of this picture of MRI triggering (Zhu et al. 2007, 2009a); this means that transport in the innermost disk is

Table 3
Fit to Zhu et al. (2007, 2008) Opacity but with Opacity from Water Ice, Graphite, and Silicate Dust Included[a]

$\log_{10} T$	$\log_{10} \kappa$	Comments
$<0.019 \log_{10} P + 2.14$	$1.5 \log_{10} T - 2.48$	Water ice opacity
$<0.019 \log_{10} P + 2.21$	$-3.53 \log_{10} T + 0.095 \log_{10} P + 8.29$	Water ice evaporation
<2.79	$1.5 \log_{10} T - 2.84$	Metal grain opacity
<2.97	$-5.83 \log_{10} T + 17.7$	Graphite corrosion
$<0.027 \log_{10} P + 3.16$	$2.13 \log_{10} T - 5.94$	Grain opacity
$<0.0281 \log_{10} P + 3.19$	$-42.98 \log_{10} T + 1.312 \log_{10} P + 135.1$	Silicate grain evaporation
$<0.03 \log_{10} P + 3.28$	$4.063 \log_{10} T - 15.013$	Water vapor
$<0.00832 \log_{10} P + 3.41$	$-18.48 \log_{10} T + 0.676 \log_{10} P + 58.93$	
$<0.015 \log_{10} P + 3.7$	$2.905 \log_{10} T + 0.498 \log_{10} P - 13.995$	Molecular opacities
$<0.04 \log_{10} P + 3.91$	$10.19 \log_{10} T + 0.382 \log_{10} P - 40.936$	H scattering
$<0.28 \log_{10} P + 3.69$	$-3.36 \log_{10} T + 0.928 \log_{10} P + 12.026$	Bound–free, free–free
Else[a]	−0.48	Electron scattering

Notes.
[a] Both C and Fortran subroutine can be downloaded at http://www.astro.princeton.edu/~zhzhu/opacity.html.
[b] With one additional condition to set the boundary: if $\log_{10}\kappa < 3.586 \log_{10} T - 16.85$ and $\log_{10} T < 4$, $\log_{10}\kappa = 3.586 \log_{10} T - 16.85$.

almost certainly dominated by magnetic turbulence rather than gravitational instability, and the symmetry of the rotationally broadened line profiles (e.g., Zhu et al. 2009a) yields no evidence for a strong departure from axisymmetry as would be expected for pure clump accretion.

It is worth emphasizing that we find some clumps that can shear out (be tidally destroyed) as they migrate to the innermost disk regions if they do not open gaps and slow down their migration. Thus, simply finding fragmentation and inward migration is no guarantee that a clump will actually accrete onto the central star as an entity; it is necessary to follow the evolution of the mass inside of 1 AU, which no simulations have done successfully yet, and consider the potential if not probable effects of magnetic turbulence in addition to GI. It may be, however, that the tidal destruction of the clumps produced by GI-induced fragmentation (Boley et al. 2010) or the episodic nature of the GI accretion (Boley & Durisen 2008) can serve as a mechanism to transport mass to AU scales (compared with the steady accretion by GI as suggested by Armitage et al. 2001 and Zhu et al. 2009b, 2009c) to trigger the MRI.

On the other hand, these outbursts can affect disk fragmentation. Recently, Stamatellos et al. (2011b) have pointed out that the episodic accretion from Zhu et al. (2010a) can significantly affect the low mass end of the stellar initial mass function.

8. CONCLUSIONS

We have presented 2D hydrodynamic simulations of self-gravitating protostellar disks subject to axisymmetric, steady mass loading from an infalling envelope and irradiation from the central star to explore the growth of GI, fragmentation, and the fragmented clump evolution. Our results can be summarized as follows.

1. We confirm previous analytic estimates that at high infall rates there is a critical disk radius for infall $\sim$50 AU, beyond which disk fragmentation occurs. This critical radius decreases with increasing mass accretion rate.
2. At low infall rates, irradiation suppresses fragmentation and pushes the critical radius to larger values. For a solar-mass protostar, this critical radius is 200 AU if the infall rate is $\lesssim 10^{-5}\,M_\odot\,\mathrm{yr}^{-1}$.
3. With the gradual addition of the mass to the disk from the infall, our simulations converge with the increasing numerical resolution for both fragmentation and non-fragmentation cases.
4. The disk critical fragmentation α parameter seems to be larger than that found by previous work; we suggest this is due to differences in the infall model, the thermal history of the disk, and the radiative energy trapping of the clumps.
5. For fragmenting disks, the clumps form at a mass that is close to (in some cases slightly smaller than) the mass in the initial disk contained within the typical GI length scale. Rotational support becomes increasingly important as the clump collapses and accretes high angular momentum material from the disk.
6. The clumps accrete from the disk at a rate $\dot{M}_c \sim 4\Sigma r_H^2\Omega$, which can be understood by assuming the accretion cross section corresponds to 1–2 Hill radii. In our irradiated disks, this is 10^{-5}–$10^{-4}\,M_\odot\,\mathrm{yr}^{-1}$, suggesting the clump can accrete to subsolar mass on the timescale of thousands of years.
7. The clumps migrate inward on the typical type I timescale ($\sim 2\times10^3$ yr in our models) initially, but with a stochastic component superposed because of interaction with the background spiral waves. However, the clump slows down when its mass is comparable to the local disk mass due to its inertia. A simple fit is given that agrees well with the simulation results.
8. When a clump migrates inward its Hill radius decreases. Accretion by the clump, however, counteracts the effect of the migration and slows the shrinking of the Hill radius.
9. There are at least two distinct fates of the clumps, depending on the migration speed. If the clump migrates slowly with enough time to cool, shrink, and accrete, it can become massive enough to open a gap ($M_c > 0.1\,M_\odot$ in our models). This slows down its migration (transition to type II migration) and may lead to the formation of a binary companion (3 out of 13 clumps in our simulation). On the other hand, if the clump migrates inward quickly, and is not massive enough to open a gap, it is subject to tidal destruction (4 out of 13 clumps). In the long run, however, the massive, gap-opening clump should be the final fate for these disks, since new clumps can continue forming and be quickly tidally destroyed until eventually a massive clump forms, opens a gap, and remains in the disk for a long period of time.
10. A simple analytic clump evolution model with clump accretion, migration, and cooling included is presented and confirms that the different clump fates depend on the migration and accretion rates.
11. Both rapid clump migration and rapid gas accretion (leading to clumps much more massive than giant planets) pose challenges to the scenario that giant planets are formed in situ by GI. It is even more challenging to explain currently found giant planets beyond 50 AU around A-type stars, since, under stronger irradiation, the fragmented clumps will be more massive than those produced in our simulations. On the other hand, GI fragmentation can provide a formation mechanism for close binary systems.
12. The first cores produced by GI-induced fragmentation can be as large as 10 AU when the core is at 100 AU. Its luminosity can be as high as $0.1\,L_\odot$ if the core mass is $0.1\,M_\odot$, or $0.002\,L_\odot$ if the core mass is 10 M_J. With an effective temperature around 100 K, these clumps can be easily detected and resolved by ALMA, although these first cores may only exist for thousands of years before they collapse to form the second core.
13. Although accretion of discrete clumps does not agree with observational constraints on FU Ori objects, tidal destruction can serve as a mechanism to add a stochastic component to mass buildup in the inner disk, potentially varying the resulting MRI-triggered outburst.

This work was supported in part by NASA grant NNX08AI39G from the Origins of Solar Systems program, and in part by the University of Michigan. We thank Aaron Boley for helpful discussion during the Gordon conference and Sergei Nayakshin for giving us comments after reading our initial draft. Particularly, we thank the referee for a very detailed and helpful report. The simulation work reported here was initiated during the research programme Dynamics of Discs and Planets hosted by the Isaac Newton Institute in 2009. Thanks again to Jeremy Hallum for maintaining the compute cluster on which these simulations were performed.

APPENDIX A

OPACITY TABLE

The low-temperature opacity is important for disk fragmentation. Thus, we have updated our low-density opacity in Zhu et al. (2009), including water ice, carbonate, and silicate grains. The opacity fits are given in Table 3.

The dust grain size distribution is chosen to be a power law with slope 3.5 from 0.005 to 1 μm. Olivine silicate to gas mass ratio is 0.0017, pyroxene silicate to gas mass ratio is 0.0017, graphite to gas mass ratio is 0.0041, and water ice to gas mass ratio is 0.0056. We use the dust destruction boundary as in D'Alessio et al. (2001).

APPENDIX B

BOUNDARY CONDITIONS

We improve the boundary conditions of the publicly available version of FARGOADSG so that the disk is in pressure equilibrium at the boundary. Take the inner boundary as an example. Assuming the disk surface density distribution has the same slope with radii in the ghost zone and the computational zone, we extrapolate the density (Σ) and internal energy (E) of the first two computational zones to the ghost zone as

$$\log(\eta_{g,j}/\eta_{1,j}) = \frac{\log(\bar{\eta_1}/\bar{\eta_2})}{\log(R_1/R_2)}(\log(R_g/R_1)), \quad \text{(B1)}$$

where $\eta_{i,j}$ is the density or the internal energy at the grid with radial number i and azimuthal number j and $\bar{\eta_1}$ and $\bar{\eta_2}$ are the azimuthal averaged value at the first and second radii.

Then the azimuthal velocities of the ghost zone are calculated by

$$u_\phi^2 = \frac{E(\gamma-1)}{\Sigma}\frac{\partial \log E}{\partial \log R} + \frac{R\partial\Phi}{\partial R}, \quad \text{(B2)}$$

where $R\partial\Phi/\partial R$ is just the GM/R_g and $\partial \log E/\partial \log R$ is given above. The radial velocity of the ghost zone equals to that of the first computation zone only if the radial velocity is inward, otherwise it is 0.

With this treatment, we can reproduce the accretion rate of an axisymmetric disk quite well without over-predicting the mass accretion rate as the normal free-flow boundary condition leads to. However, the extrapolation may lead to a negative density and energy value in the ghost zone if the disk's density and energy fluctuate significantly close to the inner boundary. This becomes more severe if a clump forms in the disk and migrates close to the inner boundary. Thus for the fragmenting disks, we have also carried simulations with normal outflow boundary condition (Stone & Norman 1992).

APPENDIX C

RADIATIVE CORE LUMINOSITY–MASS RELATION

Assuming a radiative core (as our 2D simulations implicitly assume in Equation (4)), with the uniform energy source model and "radiative zero" solution, the clump structure can be approximated by a polytrope $P = K' T^{n_e+1}$ (Cox 1968, chap. 23.3), where $n_e = -a+3 = 1.5$ and a is the slope of the opacity on temperature ($\kappa = \kappa_0 T^a$). The uniform energy source model should afford a fairly good approximation of gravitationally contracting stars (Cox 1968, chap. 17). The structure of the polytropic sphere can be solved by the Lane–Emden equation. A radiative sphere with zero-temperature boundary condition has luminosity

$$L_c = \frac{64\pi\sigma}{3\kappa_0}\left(\frac{G}{\Re}\right)^{-a+4}\frac{1}{n_e+1}\left[\frac{4\pi}{(n_e+1)^{n_e}\xi^{n_e+1}(-\theta'^{n_e}_1)^{n_e-1}}\right]^{(-a+3)/n_e} \times \frac{\mu^{-a+4}M_c^{-a+3}}{r_c^{-a}}, \quad \text{(C1)}$$

where σ is the Stefan–Boltzmann constant. For dust opacity $a = 1.5$ in Appendix A. The above equation is

$$L_c = \frac{64\pi\sigma}{3\kappa_0}\left(\frac{G\mu}{\Re}\right)^{2.5}\frac{0.424^{1.5}M_c^{1.5}}{2.5r_c^{-1.5}}. \quad \text{(C2)}$$

With our opacity this can be reduced to

$$L_c = 2\times10^{-5}\,L_\odot\left(\frac{M_c}{M_\odot}\frac{r_c}{R_\odot}\right)^{1.5} = 2\times10^{-3}\,L_\odot\left(\frac{M_c}{0.01\,M_\odot}\frac{r_c}{10\,\mathrm{AU}}\right)^{1.5}. \quad \text{(C3)}$$

The clump central temperature, pressure, and density are (notation as in Cox 1968, chap. 23.1, and $n = n_e = 1.5$, so $\xi_1 = 3.65375$ and $-\xi_1^2\theta_1' = 2.71406$)

$$T_c = \frac{1}{(n_e+1)(-\xi\theta')_1}\frac{G}{\Re}\frac{\mu M_c}{r_c} = 1.234\times10^7\frac{\mu M_c/M_\odot}{r_c/R_\odot}\,\mathrm{K} = 138\frac{M_c/0.01\,M_\odot}{r_c/10\,\mathrm{AU}}\,\mathrm{K}, \quad \text{(C4)}$$

with $\mu = 2.4$,

$$P_c = \frac{1}{4\pi(n_e+1)(\theta')_1^2}\frac{GM_c^2}{r_c^4} = 0.08658\times10^{17}\frac{(M_c/M_\odot)^2}{(r_c/R_\odot)^4}\,\mathrm{dyne\,cm^{-2}}, \quad \text{(C5)}$$

$$\rho_c = (1/3)(-\xi/\theta')_1\bar{\rho} = 5.99071\frac{M_c}{4/3\pi r_c^3}. \quad \text{(C6)}$$

From Equation (C4) we can derive

$$\frac{GM_c}{\Re r_c T_c} = \frac{1}{\mu 0.537}. \quad \text{(C7)}$$

With $\mu = 2.4$, we can derive $GM_c/\Re r_c T_c = 0.7759$.

On the other hand, for a completely convective core, $d\ln T/d\ln P = (\Gamma_2-1)/\Gamma_2$. With the ideal equation of state for diatomic gas (T is high enough that both the rotational and vibrational modes are active), $\Gamma_2 = \gamma = 7/5$. Assuming Γ_2 is constant throughout the core, integrating $d\ln T/d\ln P$ from the core surface to the center leads to $P = K' T^{n_e+1}$ with $n_e = 1/(\gamma-1) = 2.5$. The clump structure is represented by a polytrope $P = K' T^{3.5}$ which is steeper than our radiative case (in stellar cases with monatomic gas, $n = 1.5$, which is the same as our radiative cores). With $n_e = 2.5$, we have $\xi_1 = 5.35528$ and $-\xi_1^2\theta_1' = 2.18720$. Thus, the central temperature, pressure, and density are

$$T_c = 1.603\times10^7\frac{\mu M_c/M_\odot}{r_c/R_\odot}\,\mathrm{K} = 179\frac{M_c/0.01\,M_\odot}{r_c/10\,\mathrm{AU}}\,\mathrm{K}, \quad \text{(C8)}$$

with $\mu = 2.4$,

$$P_c = 0.4935 \times 10^{17} \frac{(M_c/M_\odot)^2}{(r_c/R_\odot)^4} \,\mathrm{dyne\,cm^{-2}}\,, \tag{C9}$$

$$\rho_c = 23.41 \frac{M_c}{4/3\pi r_c^3}\,. \tag{C10}$$

The K' in the polytrope can be derived using Equations (C4) and (C5):

$$K' = \Re^{n_e+1} \left(\frac{n_e+1}{G}\right)^{n_e} \frac{\xi_1^{n_e+1}(-\theta')_1^{n_e-1}}{4\pi} \frac{1}{\mu^{n_e+1} M_c^{n_e-1} r_c^{3-n_e}}, \tag{C11}$$

$$K' = \left(\frac{3.5}{G}\right)^{2.5} \Re^{3.5} \frac{5.3554^{3.5} 0.07626^{1.5}}{4\pi} \frac{1}{\mu^{3.5} M_c^{1.5} r_c^{0.5}}\,, \tag{C12}$$

which is

$$K' = \frac{13.65\Re^{3.5}}{\mu^{3.5} M_c^{1.5} r_c^{0.5} G^{2.5}}\,. \tag{C13}$$

However, the luminosity is determined by the boundary where the convective core becomes radiative. For a fully convective core, we assume this occurs at the photosphere where the optical depth $\tau = 2/3$. The pressure at the photosphere is

$$P_{\rm eff} = \frac{\rho_{\rm eff} \Re T_{\rm eff}}{\mu} \sim \frac{2g}{3\kappa_R} = \frac{2g}{3\kappa_0 T_{\rm eff}^a}\,. \tag{C14}$$

Thus,

$$\rho_{\rm eff} = \frac{2\mu g}{3\kappa_0 \Re T_{\rm eff}^{a+1}}\,. \tag{C15}$$

Then with

$$\frac{P_{\rm eff}}{T_{\rm eff}^{7/2}} = \frac{\rho_{\rm eff}\Re T_{\rm eff}}{\mu T_{\rm eff}^{7/2}} = K'\,, \tag{C16}$$

we can derive

$$T_{\rm eff} = (20.48\kappa_0)^{-1/(a+3.5)} \left(\frac{G\mu}{\Re}\right)^{3.5/(a+3.5)} \times r_c^{-1.5/(a+3.5)} M_c^{2.5/(a+3.5)}\,. \tag{C17}$$

And the luminosity is

$$L = 4\pi\sigma\,(20.48\kappa_0)^{-4/(a+3.5)} \left(\frac{G\mu}{\Re}\right)^{14/(a+3.5)} \times r_c^{(2a+1)/(a+3.5)} M_c^{10/(a+3.5)}\,. \tag{C18}$$

With $a = 1.5$,

$$L = 4\pi\sigma\,(20.48\kappa_0)^{-4/5} \left(\frac{G\mu}{\Re}\right)^{14/5} r_c^{4/5} M_c^2\,. \tag{C19}$$

With our opacity this is

$$L_c = 1.715 \times 10^{-3}\, L_\odot \left(\frac{M_c}{0.01\,M_\odot}\right)^2 \left(\frac{r_c}{10\,\mathrm{AU}}\right)^{0.8}, \tag{C20}$$

which is close to the estimate by Equation (C3) at 0.01 $M_\odot$ and 10 AU size but with the different dependence on M_c and r_c.

APPENDIX D

ANALYTIC ESTIMATE FOR THE CRITICAL FRAGMENTATION RADIUS

The parameter space for GI disk fragmentation has been explored analytically by several authors (Rafikov 2005, 2007, 2010; Levin 2007; Kratter et al. 2008, 2010a; Cossins et al. 2010; Zhu et al. 2010a). The effects of the irradiation and opacity have been discussed in detail in Rafikov (2009) and Cossins et al. (2010). Here we will give a short review on these analytic results, so that we can compare them with our numerical simulations.

To calculate the fragmentation radius at different infall rates analytically, we follow Rice et al. (2005) in using the α condition for fragmentation instead of using the cooling time condition (Gammie 2001). The α parameter is the scaling factor in the Shakura & Sunyaev (1973) treatment of viscosity, $\nu = \alpha c_s^2/\Omega$.

Rice et al. (2005) has shown that for a variety of values of specific heat ratios ($\gamma = 5/3$, 7/5, 2), for non-irradiated disks, $\alpha > \alpha_c \sim 0.06$ is the condition for fragmentation and is equivalent to cooling fragmentation condition by Gammie (2001). For irradiated disks α_c decreases with stronger irradiation (Rice et al. 2011). If the energy balance of the GI disk is local,

$$\alpha\Omega c_s^2 \Sigma \sim 2\Lambda_c\,, \tag{D1}$$

where Λ_c represents the cooling of the excess generated energy due to GI heating beyond irradiation heating (defined in Equation (4)); then

$$t_{\rm cool} \equiv c_s^2\Sigma/\Lambda_c \sim \frac{1}{\alpha\Omega}\,. \tag{D2}$$

In this case if there is a critical fragmentation $t_{\rm cool}$, it corresponds to a critical α (Rice et al. 2011). Here, we will argue why $t_{\rm cool} \equiv c_s^2\Sigma/\Lambda_c$ is the relevant cooling timescale for fragmentation in irradiated disks, instead of $c_s^2\Sigma/F$ where F is the total outward flux, even though these two definitions degenerate in non-irradiated disks. There are two heating sources in the disk: heating due to GI and heating due to the irradiation. The total outward flux F from the disk surface also consists of two parts: the part corresponding to the net cooling (Λ_c) of the energy generated by GI and the part balancing the irradiation. Consider a gas parcel in the spiral arm collapses due to its self-gravity, this gas parcel gets heated up by the compression. Whether this collapse can continue or not depends on how fast the compressed heat can be cooled (as Λ_c in Equation (4) describes), so that the net cooling ability (Λ_c) determines the fragmentation instead of the total outward flux from the disk. In the extreme case for a locally isothermal disk, Λ_c is infinite, so that $t_{\rm cool}$ defined in Equation (D2) is 0, and the disk fragments.

With our definition of $t_{\rm cool}$, α and $t_{\rm cool}$ are directly related and no assumption about the irradiation is needed. In the following derivation, we just use the critical α_c as the criterion for the fragmentation in our analytic estimate.

Since $\alpha = \dot{M}G/2c_s^3$ for a $Q = 1.5$ steady accretion disk with accretion rate $\dot{M}$ and c_s, the disk can fragment if

$$\dot{M}G/2c_s^3 > \alpha_c\,. \tag{D3}$$

Since the disk temperature that determines c_s decreases with radii, there is a critical radius (R_f) beyond which Equation (D3) is satisfied and the disk will fragment for a given $\dot{M}$. This critical radius has been derived by several authors before (Levin 2007; Rafikov 2005, 2009; Clarke 2009; Cossins et al. 2010; Kratter

et al. 2010a; Zhu et al. 2010a). In order to explore its properties and compare with our numerical simulations, we summarize previous derivations and results below briefly.

Before R_f is determined, the relationship between $\dot{M}$ and the disk sound speed c_s at disk radius R needs to be derived first. $\dot{M}$, $T_{\rm eff}$, and R for a steady accretion disk with zero torque inner boundary are related as

$$T_{\rm eff}^4 = \frac{3GM_*\dot{M}}{8\pi R^3\sigma}\left(1-\frac{R_*}{R}\right). \quad \text{(D4)}$$

$T_{\rm eff}$ and T_c are related as

$$T_{\rm eff}^4 = \frac{8}{3}\left(T_c^4 - T_{\rm ext}^4\right)\frac{\tau}{1+\tau^2}, \quad \text{(D5)}$$

where $\tau = \Sigma\kappa(T_c, \rho_c)/2$ and $\rho_c = \Sigma/2H$. Substituting Σ with T_c by assuming $Q \equiv c_s\Omega/\pi G\Sigma \sim 1.5$, T_c can be solved by equating Equations (D4) and (D5) with the Newton–Raphson method at a given $\dot{M}$. Finally, with the derived $\dot{M}$–T_c, the critical fragmentation radii (R_f) can be solved from Equation (D3) for any given α_c (the results are shown as curves in Figure 2).

The analytical solution of the optically thick limit and the irradiation-dominated limit are summarized below.

With the fragmentation condition assumption $\dot{M}G/2c_s^3 > \alpha_c$, and $T_c = T_{c,0}(R/R_0)^\gamma$, the disk will fragment if

$$\frac{R}{R_0} > \frac{R_f}{R_0} = \left(\frac{\dot{M}G}{2\alpha_c c_{s,0}^3}\right)^{2/3\gamma}, \quad \text{(D6)}$$

where $c_{s,0}$ is the sound speed at $T_{c,0}$. In the special case where $\gamma = 0$ ($T_c = T_{c,0}$, e.g., constant irradiation temperature at every radius), Equation (D6) is not valid, and the disk will fragment everywhere if and only if $\dot{M} > 2\alpha_c c_s^3/G$, independent of the disk radius (horizontal part of the curve in Figure 2 at large radii). However, we want to point out that α_c depends on the irradiation strength (Rice et al. 2011) and in this paper we assume α_c is a constant. Thus, the key parameter to define the fragmentation radii (R_f) is the temperature slope γ which will be derived as follows.

In the viscous heating-dominated limit, $T_c^4 = 3/16\ T_{\rm eff}^4\ \Sigma\kappa$, assuming the disk is optically thick which will be justified later. Considering the Rosseland mean opacity $\kappa = \kappa_r(T_c/T_r)^a$ (T_r is some arbitrary temperature to scale the opacity and $c_{s,r}$ is its corresponding sound speed), $T_{\rm eff}^4 = 3GM_*\dot{M}/8\pi R^3\sigma$, and the Toomre Q parameter of gravitationally unstable disk ($Q = c_s\Omega/\pi G\Sigma$) is close to some critical value $Q_c \sim 1.5$, we have

$$T_c = T_r\left[\frac{3}{16}\frac{3GM_*\dot{M}}{8\pi R_{d,0}^3\sigma T_r^4}\frac{c_{s,r}\Omega_0\kappa_r}{\pi G Q_c}\right]^{2/(7-2a)}\left(\frac{R}{R_{d,0}}\right)^{-9/(7-2a)}. \quad \text{(D7)}$$

Please note that $R_{d,0}$ here could be any value since it is actually canceled out. We keep it here to separate R from the square bracket, but try to maintain the other dimensionless parameters.

With the dust opacity given in Appendix A, $a = 1.5$, the midplane temperature has slope $\gamma = -9/(7\text{–}2a) = -2.25$ ($T_c \propto R^{-2.25}$). If we plug Equation (D7) into $\dot{M}G/2c_s^3 > \alpha_c$, we can derive that the disk will fragment if

$$\frac{R}{R_0} > \left(\frac{\dot{M}G}{2c_{s,r}^3\alpha_c}\right)^{-(14-4a)/27}\left[\frac{3}{16}\frac{3GM_*\dot{M}}{8\pi R_{d,0}^3\sigma T_r^4}\frac{c_{s,r}\Omega_0\kappa_r}{\pi G Q_c}\right]^{2/9}. \quad \text{(D8)}$$

Thus, with the opacity given above, we have

$$R_f \propto \alpha_c^{0.3}\dot{M}^{-0.07}M_*^{1/3}\kappa_r^{2/9}. \quad \text{(D9)}$$

R_f has a very weak dependence on $\dot{M}$. This has clearly been shown in Figure 2 where R_f is almost vertical at ~50 AU as long as the disk accretion rate is high and is viscously heating dominated. The effect of the opacity is also apparent: if the opacity depletes by a factor of 1000 (κ_r is 0.001 of the nominal value), R_f decreases by a factor of 5 (~10 AU). Finally, we will justify why we assume optically thick limit for the viscous heating-dominated cases. If we plug in the opacity law $\kappa = \kappa_r(T_c/T_r)^a$ and the disk midplane temperature $T_c = T_{c,0}(R/R_{d,0})^\gamma$ into the Toomre Q parameter, we can derive that the disk is optically thick if $R < R_t$, where R_t is

$$\left(\frac{R_t}{R_0}\right)^{3/2-\gamma(a+1/2)} = \frac{c_{s,0}\Omega_0\kappa_0}{\pi G Q}, \quad \text{(D10)}$$

where 0 denotes the corresponding physical quantities at radius R_0. Assuming $T_0 = 220$ K at $R_0 = 1$ AU, and $\gamma = -0.5$, R_t is 80 AU, which is larger than the fragmentation radius of the viscous-dominated cases ~50 AU. Thus, it is justified that the disk is optically thick at the fragmentation radius.

For the central star irradiation-dominated case, $T_c = T_{\rm irr}$. Thus with $T_{\rm irr}^4 = f(R)L/(4\pi R^2\sigma)$, we have $\gamma = -1/2$ so that

$$R_f = \left(\frac{\dot{M}G}{2\alpha_c}\right)^{-4/3}\left(\frac{k}{\mu m_h}\right)^2\left(\frac{f(R)L}{4\pi\sigma}\right)^{1/2}. \quad \text{(D11)}$$

Considering $L/L_\odot \sim (M_*/M_\odot)^2$, we can derive

$$R_f \propto (\dot{M}/\alpha_c)^{-4/3}M_*, \quad \text{(D12)}$$

thus, R_f sensitively depends on $\dot{M}$ as shown in Figure 2. In this limit, R_f does not depend on the opacity. If $T_{\rm irr} = $ const., which is similar to the envelope irradiation case, the disk will fragment everywhere as long as $\dot{M} > 2c_{s,\rm irr}^3\alpha_c/G$ (where $c_{s,\rm irr}$ is the sound speed at $T_{\rm irr}$, this $\dot{M}$ is represented as the horizontal dotted line in Figure 2), below which the disk will not fragment at any radius.

REFERENCES

Armitage, P. J. 2011, ARA&A, 49, 195
Armitage, P. J., Livio, M., & Pringle, J. E. 2001, MNRAS, 324, 705
Ayliffe, B. A., & Bate, M. R. 2009, MNRAS, 397, 657
Baruteau, C., & Masset, F. 2008, ApJ, 678, 483
Baruteau, C., Meru, F., & Paardekooper, S.-J. 2011, MNRAS, 416, 1971
Bodenheimer, P., Grossman, A. S., Decampli, W. M., Marcy, G., & Pollack, J. B. 1980, Icarus, 41, 293
Boley, A. C. 2009, ApJ, 695, L53
Boley, A. C., & Durisen, R. H. 2008, ApJ, 685, 1193
Boley, A. C., Hartquist, T. W., Durisen, R. H., & Michael, S. 2007, ApJ, 656, L89
Boley, A. C., Hayfield, T., Mayer, L., & Durisen, R. H. 2010, Icarus, 207, 509
Boley, A. C., Mejía, A. C., Durisen, R. H., et al. 2006, ApJ, 651, 517
Boss, A. P. 1997, Science, 276, 1836
Bryden, G., Chen, X., Lin, D. N. C., Nelson, R. P., & Papaloizou, J. C. B. 1999, ApJ, 514, 344
Burkert, A., & Bodenheimer, P. 1993, MNRAS, 264, 798
Cai, K., Durisen, R. H., Boley, A. C., Pickett, M. K., & Mejía, A. C. 2008, ApJ, 673, 1138
Cassen, P., & Moosman, A. 1981, Icarus, 48, 353
Cha, S.-H., & Nayakshin, S. 2011, MNRAS, 415, 3319
Chiang, E. I., & Goldreich, P. 1997, ApJ, 490, 368
Clarke, C. J. 2009, MNRAS, 396, 1066

Clarke, C. J., Harper-Clark, E., & Lodato, G. 2007, MNRAS, 381, 1543
Cossins, P., Lodato, G., & Clarke, C. 2010, MNRAS, 401, 2587
Cossins, P., Lodato, G., & Clarke, C. J. 2009, MNRAS, 393, 1157
Cox, J. P., & Giuli, R. T. (ed.) 1968, Principles of Stellar Structure (New York: Gordon and Breach)
D'Alessio, P., Canto, J., Calvet, N., & Lizano, S. 1998, ApJ, 500, 411
D'Angelo, G., & Lubow, S. H. 2008, ApJ, 685, 560
D'Alessio, P., Calvet, N., & Hartmann, L. 2001, ApJ, 553, 321
Durisen, R. H., Boss, A. P., Mayer, L., et al. 2007, in Protostars and Planets V, ed. B. Reipurth, D. Jewitt, & K. Keil (Tucson, AZ: Univ. Arizona Press), 607
Eisner, J. A., & Hillenbrand, L. A. 2011, ApJ, 738, 9
Forgan, D., & Rice, K. 2010, MNRAS, 406, 2549
Forgan, D., Rice, K., Stamatellos, D., & Whitworth, A. 2009, MNRAS, 394, 882
Gammie, C. F. 2001, ApJ, 553, 174
Gammie, C. F., Ostriker, J. P., & Jog, C. J. 1991, ApJ, 378, 565
Goldreich, P., Goodman, J., & Narayan, R. 1986, MNRAS, 221, 339
Harsono, D., Alexander, R. D., & Levin, Y. 2011, MNRAS, 413, 423
Hartmann, L., Cassen, P., & Kenyon, S. J. 1997, ApJ, 475, 770
Hayfield, T., Mayer, L., Wadsley, J., & Boley, A. C. 2011, MNRAS, 1351
Helled, R., & Bodenheimer, P. 2010, Icarus, 207, 503
Helled, R., & Bodenheimer, P. 2011, Icarus, 211, 939
Henon, M., & Petit, J.-M. 1986, Celest. Mech., 38, 67
Kalas, P., Graham, J. R., Chiang, E., et al. 2008, Science, 322, 1345
Kenyon, S. J., & Hartmann, L. 1987, ApJ, 323, 714
Kley, W. 1999, MNRAS, 303, 696
Kratter, K. M., Matzner, C. D., & Krumholz, M. R. 2008, ApJ, 681, 375
Kratter, K. M., Matzner, C. D., Krumholz, M. R., & Klein, R. I. 2010a, ApJ, 708, 1585
Kratter, K. M., & Murray-Clay, R. A. 2011, ApJ, 740, 1
Kratter, K. M., Murray-Clay, R. A., & Youdin, A. N. 2010b, ApJ, 710, 1375
Larson, R. B. 1969, MNRAS, 145, 271
Levin, Y. 2007, MNRAS, 374, 515
Lin, D. N. C., & Papaloizou, J. 1979, MNRAS, 186, 799
Lin, M.-K., & Papaloizou, J. C. B. 2011a, MNRAS, 415, 1445
Lin, M.-K., & Papaloizou, J. 2011b, arXiv:1112.1704
Lissauer, J. J. 1987, Icarus, 69, 249
Lubow, S. H., Seibert, M., & Artymowicz, P. 1999, ApJ, 526, 1001
Marois, C., Macintosh, B., Barman, T., et al. 2008, Science, 322, 1348
Martin, R. G., & Lubow, S. H. 2011, ApJ, 740, L6
Masset, F. S. 2000, A&A, 141, 165
Meru, F., & Bate, M. R. 2011, MNRAS, 411, L1
Michael, S., Durisen, R. H., & Boley, A. C. 2011, ApJ, 737, L42
Nayakshin, S. 2010a, MNRAS, 408, 2381
Nayakshin, S. 2010b, MNRAS, 408, L36
Nayakshin, S. 2011, MNRAS, 413, 1462
Nelson, A. F. 2006, MNRAS, 373, 1039
Nelson, R. P., Papaloizou, J. C. B., Masset, F., & Kley, W. 2000, MNRAS, 318, 18
Offner, S. S. R. 2011, in IAU Symp. 270, Computational Star Formation, ed. J. Alves, B. Elmegreen, J. Girart, & V. Trimble (Cambridge: Cambridge Univ. Press), 231
Ogilvie, G. I., & Lubow, S. H. 1999, ApJ, 515, 767
Paardekooper, S.-J., Baruteau, C., & Meru, F. 2011, MNRAS, 416, L65
Petit, J. M., & Henon, M. 1986, BAAS, 18, 763
Pickett, B. K., Durisen, R. H., Cassen, P., & Mejia, A. C. 2000, ApJ, 540, L95
Prialnik, D., & Livio, M. 1985, MNRAS, 216, 37
Rafikov, R. R. 2001, AJ, 122, 2713
Rafikov, R. R. 2005, ApJ, 621, L69
Rafikov, R. R. 2007, ApJ, 662, 642
Rafikov, R. R. 2009, ApJ, 704, 281
Rice, W. K. M., Armitage, P. J., Mamatsashvili, G. R., Lodato, G., & Clarke, C. J. 2011, MNRAS, 418, 1356
Rice, W. K. M., Lodato, G., & Armitage, P. J. 2005, MNRAS, 364, L56
Rice, W. K. M., Mayo, J. H., & Armitage, P. J. 2010, MNRAS, 402, 1740
Rogers, P. D., & Wadsley, J. 2011, MNRAS, 414, 913
Shakura, N. I., & Sunyaev, R. A. 1973, A&A, 24, 337
Stamatellos, D., Maury, A., Whitworth, A., & Andre, P. 2011, MNRAS, 413, 1787
Stamatellos, D., & Whitworth, A. P. 2008, A&A, 480, 879
Stamatellos, D., & Whitworth, A. P. 2009a, MNRAS, 392, 413
Stamatellos, D., & Whitworth, A. P. 2009b, MNRAS, 400, 1563
Stamatellos, D., Whitworth, A. P., & Hubber, D. A. 2011, ApJ, 730, 32
Stone, J. M., & Norman, M. L. 1992, ApJS, 80, 753
Tanaka, H., Takeuchi, T., & Ward, W. R. 2002, ApJ, 565, 1257
Terebey, S., Shu, F. H., & Cassen, P. 1984, ApJ, 286, 529
Vorobyov, E. I. 2011, ApJ, 728, L45
Vorobyov, E. I., & Basu, S. 2005, ApJ, 633, L137
Vorobyov, E. I., & Basu, S. 2006, ApJ, 650, 956
Vorobyov, E. I., & Basu, S. 2010, ApJ, 719, 1896
Winn, J. N., Albrecht, S., Johnson, J. A., et al. 2011, ApJ, 741, L1
Wuchterl, G. 1993, Icarus, 106, 323
Zhu, Z., Espaillat, C., Hinkle, K., et al. 2009a, ApJ, 694, L64
Zhu, Z., Hartmann, L., Calvet, N., et al. 2007, ApJ, 669, 483
Zhu, Z., Hartmann, L., Calvet, N., et al. 2008, ApJ, 684, 1281
Zhu, Z., Hartmann, L., & Gammie, C. 2009b, ApJ, 694, 1045
Zhu, Z., Hartmann, L., & Gammie, C. 2010a, ApJ, 713, 1143
Zhu, Z., Hartmann, L., Gammie, C., & McKinney, J. C. 2009c, ApJ, 701, 620
Zhu, Z., Hartmann, L., Gammie, C. F., et al. 2010b, ApJ, 713, 1134